ELSEVIER

Contents lists available at ScienceDirect

Optical Materials: X

journal homepage: www.elsevier.com/locate/omx



Invited article

Featuring a new computational protocol for the estimation of intensity and overall quantum yield in lanthanide chelates with applications to Eu(III) mercapto-triazole Schiff base ligands

Renaldo T. Moura Jr. ^{a,b}, Mateus Quintano ^a, Carlos V. Santos-Jr ^c, Vinícius A.C.A. Albuquerque ^d, Eduardo C. Aguiar ^d, Elfi Kraka ^a, Albano N. Carneiro Neto ^{e,*}

- ^a Computational and Theoretical Chemistry Group (CATCO), Department of Chemistry, Southern Methodist University Dallas, TX 75275, USA
- b Department of Chemistry and Physics Center of Agrarian Sciences, Federal University of Paraiba, Areia, PB 58397-000, Brazil
- ^c Department of Chemistry, Federal University of Paraiba, Joao Pessoa, PB 58051-970, Brazil
- ^d Academic Unity of Belo Jardim, Federal Rural University of Pernambuco, Belo Jardim, PE 55156-580, Brazil
- e Phantom-g, Physics Department and CICECO Aveiro Institute of Materials, University of Aveiro, Aveiro 3810-193, Portugal

ARTICLE INFO

Keywords: f-f intensity parameters Overall quantum yield Localized polarizability Local vibrational mode theory Eu(III) complexes Schiff base ligands

ABSTRACT

Computational studies on luminescent properties of lanthanides chelates are important for the pre-synthetic design of new luminescent materials. However, the development of suited computational methods and protocols is still in its infancy. Here we present a new computational protocol for a systematic description and analysis of luminescent properties of Ln(III) chelates. The new methodologies herein presented are divided in three major categories: (1) Utilization of local vibrational mode theory for obtaining local Ln–ligand force constants; (2) Calculation of ligand effective polarizabilities through complex localized molecular orbitals; and (3) Extended formulation of excited state donor–acceptor R_L distances accounting for excited molecular orbitals weights. The protocol was applied to understand the underlying photophysical processes in two Eu(III) complexes with mercapto-triazole Schiff bases as main ligands, utilizing time-dependent density functional theory (ω B97X-D/MWB52(Eu)/Def2-TZVP). The introduction of local force constants into lanthanide spectroscopy led to a unique explanation of the inverse relationship between the Ln–ligand strength and ligand effective polarizability. This new protocol will contribute to a better understanding of Ln–ligand bond properties, to more accurate results in terms of Judd–Ofelt intensity parameters and overall quantum yield, and will bridge the current gap between available theoretical results and experimental data.

1. Introduction

Materials based on trivalent lanthanides ions (Ln(III)) are known mainly because of their magneto-optical properties employed as biological probes [1], UV dosimeters [2], organic light emitting diodes (OLED) [3], persistent radioluminescence phosphors [4,5], nanothermometers [6,7], optical sensing and Internet of Things [8]. The f-electrons of Ln(III) ions are shielded by the filled (and more radially external) s and p subshells, leading to weak interactions with the environment. Though weak, this interaction is responsible for unfolding energy levels of the f-electrons that leads to interesting and useful Ln compounds with luminescent properties [9].

The modeling of Ln(III) luminescent properties is a multistep procedure that can be pictured as an *in silico* experiment. In fact, this computer experiment follows the usual chemical/physical experimental procedure, namely, preparation of the system, control of variables,

measurements, and analyses [9]. A wide range of different ligands (in different chemical environments) is capable of interacting with different Ln(III) ions. Polydentate ligands increase complex stability compared with their monodentate counterparts forming, in this way, the basis to highly luminescent lanthanide compounds [10]. Also, lanthanide ions have a preference for coordinating with hard Lewis bases such as oxygen and nitrogen, which are present in the main ligands, such as 2,2'-bipyridine, 1,10-phenantroline and β -diketonates [11]. The proper description of the complex molecular geometry (or solid-state structure) and the satisfactory description of Ln(III)–ligand interactions are the main challenging tasks in the modeling of energy transfer processes and photophysical properties. The theoretical methodology applied requires the proper treatment of relativistic effects, that can be included by different methodologies, namely: the Zero-Order Regular Approximation (ZORA) [12,13], the Douglas–Kroll–Hess (DKH) Hamiltonian [14,

E-mail addresses: renaldo.mourajr@cca.ufpb.br (R.T. Moura Jr.), albanoneto@ua.pt (A.N. Carneiro Neto).

^{*} Corresponding author.

Fig. 1. Schematic representation of (a) the Eu(III) complexes and (b) L2 and L5, the corresponding Schiff base ligands studied in this work. Index numbers in (a) refer to the numbering of atoms used in this work. Carbon atoms are indicated by numbers without atomic symbols and hydrogen atoms bonded to them are omitted.

15] or the Normalized Elimination of the Small Component (NESC) Method [16] and its updates and new implementations [17–20]. These methods offer different strengths and computational costs and are scalar relativistic corrections for the contraction of s- or p-orbitals and the expansion of d- or f-orbitals.

Complex geometries and electronic structure properties, such as transition states properties (energies, location, and their oscillator strengths) and vibrational frequencies are used to calculate so-called theoretical intensity parameters [21], intramolecular energy transfer (IET) rates [9] and other relevant transition rates. These rates are then used in turn to build a system of coupled rate equations [9], which is solved to provide state populations, overall quantum yield, decay lifetimes, and other luminescent properties. These procedures all rely on accurate and high quality computational data.

The present work aims at highlighting a series of improvements concerning the computational modeling of the photophysical properties of Ln(III)-based complexes. As a proof of concept, the new featured procedures highlighted here were applied to gain a better understanding of the underlying photophysical processes in two Eu(III) complexes (Fig. 1) with mercapto-triazole Schiff bases (derived from 3-nitrophenyl-4-amino-5-mercapto -1,2,4-triazole with benzil/diacety) as main ligands. Schiff bases correspond to a sub-class of imides largely used as ligands in metal complexes acting as donors to form stable metal chelates [22] with biological applications such as those employing antiviral, antifungal, antibacterial and antitumoral activities [23-26], cancer diagnosis and therapy [27], and technological applications such as OLEDs, liquid crystals and metal sensing [28-31]. Panday and collaborators recently published a series of lanthanide complexes with tetradentate mercapto-triazole Schiff bases as ligands with antibacterial and antifungal activities increased by the Ln(III) coordination [32], and sensitization of lanthanide ion [33]. Here the studied compounds was extracted from Vishwakarma and coworkers [33], that compiled a large set of Tb(III) and Eu(III) complexes with mercapto-triazole Schiff bases acting as main ligands. These authors reported emission spectra only for two types of compounds, labeled L2 in Fig. 1a and L5 in Fig. 1b [33]. As one wants to evaluate the robustness of featured methodologies, the comparison between experimental and theoretical intensity parameters is a prerequisite. To maintain consistency, here the same labels (L2 and L5) are adopted in this work. The overall quantum yields were reported as 50% and 53% for $[\mathrm{Eu}(\mathrm{L2})\mathrm{Cl}(\mathrm{H_2O})_3]$ and $[\mathrm{Eu}(\mathrm{L5})\mathrm{Cl}(\mathrm{H_2O})_3]$ compounds, respectively.

The featured new methodologies shown here are divided in three categories: 1. Utilization of the local vibrational mode theory [34] in the description of Ln(III)-ligand charge factors (through local force constants k^a) that appear in the theoretical intensity parameters; 2. Improved effective ligand polarizabilities (α') by decomposing the molecular polarizability for the entire complex into localized molecular orbitals (LMOs) contributions; and 3. New formulation of the donoracceptor distance expression (R_L — i.e. ligand excited state centroids to the Eu(III) ion) that includes different orbital excitations that compose the excited state. All new implementations are included in the JOYSpectra [35], ChemBOS [36,37], and LModeA [38] packages.

2. Methodology

2.1. Experimental data extraction

The emission spectra of the $[Eu(L2)Cl(H_2O)_3]$ and $[Eu(L5)Cl(H_2O)_3]$ complexes were taken from Ref. [33] using the WebPlotDigitizer program.¹ The area under the Eu(III) $^5D_0 \rightarrow ^7F_I$ (J = 1, 2, and 4)

^{1 (}https://automeris.io/WebPlotDigitizer/)

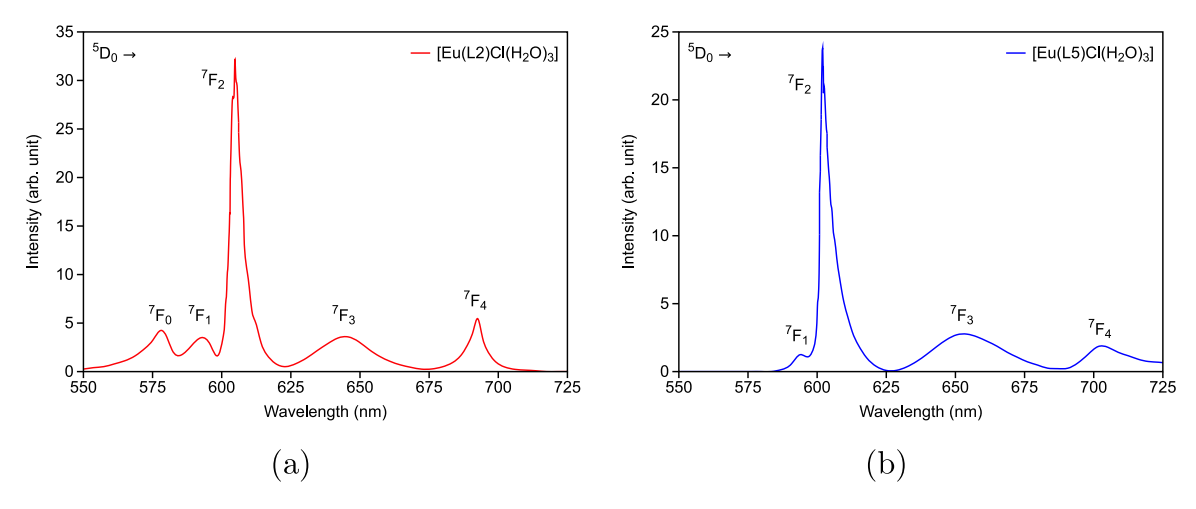


Fig. 2. Experimental emission spectra for $[Eu(L2)Cl(H_2O)_3]$ and $[Eu(L5)Cl(H_2O)_3]$ complexes. Source: Reproduced with permission from A. Vishwakarma, S.K. Sengupta, O.P. Pandey, Characterizations and photo-physical properties of synthesized Europium(III) and Terbium(III) complexes with mercapto-triazole Schiff base ligands, J. Lumin. 229 (2021) 117659. © 2021 Elsevier.

transitions (Fig. 2) are then utilized to determine the experimental intensity parameters Ω_1^{exp} :

$$\Omega_{\lambda}^{exp} = \frac{3\hbar c^3 A_{0 \to \lambda}}{4e^2 \left(\omega_{0 \to \lambda}\right)^3 \chi \left\langle {}^7F_{\lambda} \left\| U^{(\lambda)} \right\| {}^5D_0 \right\rangle^2} \tag{1}$$

where $\chi=\frac{n(n^2+2)^2}{9}$ is the Lorentz local field correction (n is the refraction index of the medium, considered as 1.5 for most Ln(III) complexes in the solid-state [9]), $\omega_{0\to\lambda}$ is the angular frequency of the ${}^5\mathrm{D}_0\to{}^7\mathrm{F}_\lambda$ ($\lambda=2$ and 4) emission, $\left\langle{}^7\mathrm{F}_\lambda\left\|U^{(\lambda)}\right\|{}^5\mathrm{D}_0\right\rangle^2$ are the squared reduced matrix elements with values 0.0032 and 0.0023 for $\lambda=2$ and 4 [39], respectively. Einstein's spontaneous emission coefficients $(A_{0\to\lambda})$ were obtained using $A_{0\to1}=50$ s⁻¹ from the magnetic dipole ${}^5\mathrm{D}_0\to{}^7\mathrm{F}_1$ emission as a reference [40]:

$$A_{0 \to \lambda} = A_{0 \to 1} \left(\frac{S_{0 \to \lambda}}{S_{0 \to 1}} \right) \tag{2}$$

where $S_{0\to\lambda}$ and $S_{0\to1}$ are the integrated areas under emission curves of the ${}^5\mathrm{D}_0 \to {}^7\mathrm{F}_\lambda$ and ${}^5\mathrm{D}_0 \to {}^7\mathrm{F}_1$ transitions, respectively. The obtained $S_{0\to2}$, $S_{0\to4}$, Ω_2^{exp} , and Ω_4^{exp} values are set out in Table **S1** (see Supplementary Material).

2.2. Theoretical intensity parameters

The theoretical intensity parameters Ω_{λ}^{theo} provide information about the chemical environment around the Eu(III) ion. As described in the literature [21,41–48], these quantities can be obtained as follows

$$\Omega_{\lambda}^{\text{theo}} = (2\lambda + 1) \sum_{\text{t,p}} \frac{\left| \mathbf{B}_{\lambda t p} \right|^2}{2t + 1}, \ \mathbf{B}_{\lambda \text{tp}} = \mathbf{B}_{\lambda t p}^{FED} + \mathbf{B}_{\lambda t p}^{DC}$$
 (3)

where

$$B_{\lambda tp}^{FED} = \frac{2}{\Delta E} \left\langle r^{t+1} \right\rangle \Theta(t, \lambda) \left(\frac{4\pi}{2t+1} \right)^{1/2} \left(\sum_{j} e^{2} \rho_{j} g_{j} \left(2\beta_{j} \right)^{t+1} \frac{Y_{p,j}^{t*}}{R_{j}^{t+1}} \right) \tag{4}$$

$$B_{\lambda tp}^{DC} = -\left[\frac{(\lambda+1)(2\lambda+3)}{(2\lambda+1)}\right]^{\frac{1}{2}} \left\langle r^{\lambda} \right\rangle \left\langle f \left\| C^{(\lambda)} \right\| f \right\rangle \left(\frac{4\pi}{2t+1}\right)^{\frac{1}{2}} \times \left(\sum_{j} \left[\left(2\beta_{j}\right)^{t+1} \alpha_{OP,j} + \alpha_{j}' \right] \frac{Y_{p,j}^{t*}}{R_{j}^{t+1}} \right) \delta_{t,\lambda+1}$$

$$(5)$$

Eq. (4) represents the forced electric dipole (FED, original Judd-Ofelt theory [46,48]) contribution in the framework of the simple

overlap model (SOM) [41,42] and Eq. (5) is the expression for the dynamic coupling contribution (DC) [43,44,47,49] in the framework of the bond overlap model (BOM) [21,50]. Both SOM and BOM take into account covalency effects.

ΔE stands for the average energy denominator method by Bebb and Gold [51,52]. The numerical factors $\Theta(t,\lambda)$ are the relation between f-g and f-d interconfigurational transitions and 4f radial integrals, assuming values of $\Theta(1,2) = -0.17$, $\Theta(3,2) = 0.34$, $\Theta(3,4) = 0.18$, $\Theta(5,4) = -0.24$, $\Theta(5,6) = -0.24$, and $\Theta(7,6) = 0.24$ [53]. g is the charge factor that, together with the overlap integral (ρ) , compose the overlap charge between the coordinating atom and the Ln(III) ion [54]. The β parameter is given by $(1 \pm \rho)^{-1}$ [41]. Y_p^{t*} are spherical harmonics, where the site environment symmetry is treated by the sum over j index (Eqs. (4) and (5)). BOM describes the ligand's polarizability in terms of α_{OP} and α' ; the former is defined as the chemical bond overlap polarizability [55] and the latter represents the ligand effective polarizability, which is related to a specific molecular region that may directly (or indirectly) affect the chemical environment of the lanthanide ion [21,50,56]. The values of α_{OP} were determined using the JOYSpectra web platform [35] as follows:

$$\alpha_{OP} = \frac{e^2 \rho^2 R^2}{2\Delta \epsilon} \tag{6}$$

where e is the electron charge, R is the bond length, ρ is the overlap integral and $\Delta \epsilon$ is the first excitation energies associated with Ln-ligating atom species [57].

The quantity g, in the context of SOM, is the charge factor that, together with the overlap integral (ρ), compose the overlap charge between the coordinating atom and the Eu(III) ion [54]. The g quantity can be evaluated as follows:

$$g = R\sqrt{\frac{k}{2\Delta\epsilon}} \tag{7}$$

where k is the force constant associated with the Ln – L atomic pair.

In previous works, a pseudo diatomic-like model [21] was applied to calculate k (and corresponding g) values. In addition, our initial approach was limited to mono and bidentate ligands. Herein we use for the first time in Eq. (7) local mode stretching force constants $k_n^a(\operatorname{Ln}-\operatorname{L})$, derived from the local vibrational mode theory (LMV), originally introduced by Konkoli and Cremer [58–62]. A comprehensive description of LMV and its applications can be found in Ref. [34] and references therein. Therefore, in the following only some highlights are summarized.

2.3. From Wilson GF formalism to the local vibrational mode theory

Applying the Wilson GF machinery, i.e., solving the Wilson equation of vibrational spectroscopy Eq. (8) [63-69] leads to normal mode frequencies, normal mode force constants and normal mode vectors expressed in normal coordinates.

$$\mathbf{F}^{x}\tilde{\mathbf{L}} = \mathbf{M}\tilde{\mathbf{L}}\boldsymbol{\Lambda} \tag{8}$$

where \mathbf{F}^x is the force constant matrix expressed in Cartesian coordinates x_i (i = 1, ... 3N). M is the diagonal mass matrix containing the atomic mass for each atom three times to account for the motion in x, y and z directions, and matrix $\tilde{\mathbf{L}}$ collects the vibrational eigenvectors $\tilde{\mathbf{I}}_{\mu}$ in its columns ($\mu=1,\ldots,N_{vib}$). The number of vibrational modes N_{vib} equals $3N - N_{tr}$ with the translational and rotational modes N_{tr} being 5 for linear and 6 for non-linear molecules. Λ is a diagonal matrix with the eigenvalues λ_{μ} , which leads to the (harmonic) vibrational frequencies ω_{μ} according to $\lambda_{\mu} = 4\pi^2 c^2 \omega_{\mu}^2$. The tilde symbol indicates mass weighting. The normal mode eigenvectors and eigenvalues are obtained by diagonalizing the force constant matrix F^x defined in Eq. (8) according to $\tilde{\mathbf{L}}^{\dagger}\mathbf{F}^{x}\tilde{\mathbf{L}} = \boldsymbol{\Lambda}$ with the normalization condition $\tilde{\mathbf{L}}^{\dagger}\mathbf{M}\tilde{\mathbf{L}} =$ I. Usually, the normal mode vectors $\tilde{\mathbf{l}}_{\mu}$ are re-normalized [63] so that Eq. (8) takes the following form

$$\mathbf{F}^{\mathbf{x}}\mathbf{L} = \mathbf{M}\mathbf{L}\boldsymbol{\Lambda} \tag{9}$$

Solution of Eq. (9) leads to the diagonal normal force constant matrix K, and the reduced mass matrix M^R in normal coordinates Q, respectively, with the dimension of matrices **K** and \mathbf{M}^R being $N_{vib} \times$ N_{vib} .

$$\mathbf{L}^{\dagger}\mathbf{F}^{x}\mathbf{L} = \mathbf{K} \tag{10}$$

$$\mathbf{L}^{\dagger}\mathbf{M}\mathbf{L} = \mathbf{M}^{R} \tag{11}$$

One can also express the molecular geometry in terms of internal coordinates q rather than Cartesian coordinates x. In this case the Wilson equation [63] becomes

$$\mathbf{F}^{q}\mathbf{D} = \mathbf{G}^{-1}\mathbf{D}\boldsymbol{\Lambda} \tag{12}$$

where **D** collects the normal mode vectors \mathbf{d}_{μ} ($\mu = 1, \dots, N_{vib}$) columnwise, and the Wilson matrix G, which is defined as

$$\mathbf{G} = \mathbf{B}\mathbf{M}^{-1}\mathbf{B}^{\dagger} \tag{13}$$

represents the kinetic energy in terms of internal coordinates. The elements of the rectangular B matrix in Eq. (13) are defined by the partial derivatives of internal coordinates q_n $(n=1,2,3\dots N_{vib})$ with regard to Cartesian coordinates x_i (i = 1, 2, 3 ... 3N),

$$\mathbf{B}_n = \frac{\delta q_n(\mathbf{x})}{\delta x_i} \tag{14}$$

The B matrix plays a central role for the Wilson equation of spectroscopy, namely connecting different sets of coordinates (internal, symmetry, curvilinear, etc.) [70-72] or Cremer-Pople ring puckering coordinates, [73] with the Cartesian coordinates. [63] Therefore, whenever a new set of coordinates is introduced, the first step is to derive the appropriate B matrix. Diagonalization of Eq. (12) leads to the equivalent of Eq. (10)

$$\mathbf{D}^{\dagger}\mathbf{F}^{q}\mathbf{D} = \mathbf{K} \tag{15}$$

The transformation to normal coordinates Q leading to the diagonal force constant matrix K collecting normal vibrational force constants and matrix **D** collecting the normal mode vectors \mathbf{d}_{μ} in internal coordinates is a standard procedure in modern quantum chemistry packages [74-76]. In particular, normal mode stretching force constants have become a popular measure of bond strength. However, caveat is appropriate. As already pointed out by Wilson in 1941 [77], normal coordinates Q are generally a linear combination of internal coordinates q or Cartesian coordinates x

$$Q_{\mu} = \sum_{j}^{N_{vib}} (\tilde{\mathbf{D}}^{\dagger} \mathbf{G}^{-1})_{\mu j} q_{j}$$

$$Q_{\mu} = \sum_{j}^{3N} (\tilde{\mathbf{D}}^{\dagger} \mathbf{G}^{-1} \mathbf{B})_{\mu j} x_{j}$$

$$(16)$$

$$Q_{\mu} = \sum_{j}^{3N} (\tilde{\mathbf{D}}^{\dagger} \mathbf{G}^{-1} \mathbf{B})_{\mu j} x_{j}$$

$$\tag{17}$$

leading to normal vibrational modes that are generally delocalized over the molecule and in this way limiting the use of normal mode frequencies and normal mode force constants as bond strength measure. For this purpose, local vibrational modes a_n and related local mode frequencies ω_n^a and force constants k_n^a are needed.

Konkoli and Cremer [34,58-62,78] derived local vibrational modes \mathbf{a}_n from the diagonal force constant matrix \mathbf{K} and the normal mode

$$\mathbf{a}_n = \frac{\mathbf{K}^{-1} \mathbf{d}_n^{\dagger}}{\mathbf{d}_n \mathbf{K}^{-1} \mathbf{d}_n^{\dagger}} \tag{18}$$

where the local mode a_n is expressed in terms of normal coordinates Oand \mathbf{d}_n is the *n*th row vector of the **D** matrix. To each local mode \mathbf{a}_n a corresponding local mode force constant k_{ij}^a

$$k_n^a = (\mathbf{d}_n \mathbf{K}^{-1} \mathbf{d}_n^{\dagger})^{-1}, \quad \mathbf{d}_n = \mathbf{B}_n \mathbf{L}$$
 (19)

and local mode frequency ω_n^a can be defined:

$$\omega_n^a = \frac{1}{2\pi c} \sqrt{\frac{k_n^a}{m_n^a}},\tag{20}$$

The local mode mass m_n^a of mode n is given by

$$m_n^a = 1/G_{n,n} = (\mathbf{b}_n \mathbf{M}^{-1} \mathbf{b}_n^{\dagger})^{-1}$$
 (21)

where $G_{n,n}$ is the nth diagonal element of the Wilson **G** matrix. For a chemical bond A-B, Eq. (21) leads to $M_A M_B / (M_A + M_B)$, which has the same form as the reduced mass of diatomic molecules.

There exists an important one-to-one relationship for each complete set of local vibrational modes and normal vibrational modes, the adiabatic connection scheme (ACS) [79], which is based on the Decius compliance matrix [80], $\Gamma = (\mathbf{F}^q)^{-1}$, defined as the inverse of the Hessian matrix in internal coordinates, and the Wilson G matrix, $\mathbf{G} = \mathbf{B}_n \mathbf{M}^{-1} \mathbf{B}_n^{\dagger}$, which is called *inverse kinetic energy* matrix [63]:

$$(\mathbf{G}_d + \lambda \mathbf{G}_{od})\mathbf{R}_{\lambda} = (\mathbf{\Gamma}_d + \lambda \mathbf{\Gamma}_{od})\mathbf{R}_{\lambda}\mathbf{\Lambda}_{\lambda},\tag{22}$$

where \mathbf{G}_d and $\mathbf{\Gamma}_d$, and \mathbf{G}_{od} and $\mathbf{\Gamma}_{od}$ are the diagonal and off-diagonal parts of Decius and Wilson matrices, respectively [63]. The matrix Λ collects the harmonic vibrational frequencies and $\mathbf{R} = \mathbf{\Gamma}^{-1}\mathbf{D}$. The parameter λ adiabatically converts the local vibrational modes ($\lambda = 0$) into their normal mode counterpart ($\lambda = 1$).

This one-to-one relationship provides the platform for a new way of analyzing vibrational spectra, the so-called decomposition of normal vibrational mode (CNM) procedure in which each normal vibrational mode l_u is decomposed into local mode contributions [34,59, 81–84]. For this purpose the local modes \mathbf{a}_n in internal coordinates are transformed d into their Cartesian coordinate counterparts \mathbf{a}_n^x via

$$\mathbf{a}_{n}^{x} = \mathbf{L}\mathbf{a}_{n} = \mathbf{L}\frac{\mathbf{K}^{-1}\mathbf{d}_{n}^{\dagger}}{\mathbf{d}_{n}\mathbf{K}^{-1}\mathbf{d}_{n}^{\dagger}}$$
(23)

Then the overlap $S_{n\mu}$ is the overlap between each local mode vector \mathbf{a}_n^{x} and a normal mode vector \mathbf{l}_u is calculated according to

$$C_{n\mu} = \frac{S_{n\mu}}{N_{vib}}, \qquad (24)$$

$$\sum_{m} S_{m\mu}$$

and
$$S_{n\mu} = \frac{(\mathbf{a}_n^{\mathbf{x}}, \mathbf{l}_{\mu})^2}{(\mathbf{a}_n^{\mathbf{x}}, \mathbf{a}_n^{\mathbf{x}})(\mathbf{l}_{\mu}, \mathbf{l}_{\mu})},$$
 (25)

with the metric (a, l) given by

$$(\mathbf{a}, \mathbf{l}) = \sum_{i,j} a_i F_{i,j}^x l_j, \tag{26}$$

where $F_{i,j}^{x}$ are elements of the Hessian matrix \mathbf{F}^{x} in Cartesian coordi-

2.4. Ligand effective polarizabilities

The bond overlap model [43,44,47] describes the chemical environment of Dynamic Coupling (DC) mechanism via overlap and ligand effective polarizabilities ($\alpha = \alpha' + \alpha_{OP}$). While α_{OP} describes the bond overlap polarization capability, α' represents ligands polarizability contributions to the DC mechanism [21,50]. Previous BOM applications were performed considering ligands as isolated molecules [21,56,85], where the Canonical Molecular Orbitals were localized to generate a set of localized molecular orbitals (LMO). LMOs are convenient to extract chemical relationship in the sense of how specific ligand portions influence the interaction with Ln(III), and their usage represents a significant improvement of the description of 4f-4f transitions intensities in the DC mechanism. However, considering ligands as isolated molecules, even taking their geometry in the complex decreases the quality of α' as a descriptor of chemical environment by introducing the lack of the Ln-L interaction.

The molecular polarizability can be decomposed in LMO contributions [21,86] in a procedure available in GAMESS package [87]. To expand the applicability of methods and capabilities exclusively available as part of the Gaussian package, here is presented a toolkit that utilizes Gaussian [88], MultiWFN [89], and ChemBOS [36,37] programs as an alternative procedure.

Algorithm 1 summarizes the procedure adopted in our implementations to integrate ChemBOS, JOYspectra, and Gaussian environments.

Algorithm 1 Pseudocode for Ligand Effective Polarizability Obtention

procedure Calculating LMOs polarizabilities from Gaussian

Single-points with E-field $(x,y,z) \leftarrow Input generator$ from input.gjf*E-field breaks wavefunction symmetry. No symmetry constraints can be imposed during SCF.

formchk output.chk -> output.fchk multiple conversion

MultiWFN $output-F_i$.fchk $\rightarrow output-F_i$ -LMO.fchk i stands for zero, x, y, and z fields

Gauss2BOS conversion tool: $output-F_i$.fchk $\rightarrow input$.bos

ChemBOS calculation: parameters ← input.bos Basis set normalization Atomic orbitals construction

Overlap and dipole matrix calculation

while $n \leq N_{LMOs}$ do $\triangleright n$ is the LMOⁿ index Put LMO₀, LMO_x, LMO_y, and LMO_z in same phase Assign LMO type: core, bond, or lone-pair Calculate LMOⁿ dipole and induced dipole vectors Calculate LMOⁿ polarizability tensor end while

Select LMOⁿ assigned to desired chemical groups Summation over desired $n \rightarrow$ forming α' for each ligand

end procedure

2.5. Intramolecular energy transfer

The intramolecular energy transfer (IET) rates from organic ligands to the Eu(III) ion were estimated by taking into consideration the dipole-dipole (W_{d-d}) , dipole-multipole (W_{d-m}) , and exchange (W_{ex}) mechanisms [9,90-93]:

$$W_{d-d} = \frac{S_L \left(1 - \sigma_1\right)^2}{(2J + 1)G} \frac{4\pi}{\hbar} \frac{e^2}{R_L^6} \sum_{\lambda} \Omega_{\lambda}^{FED} \left\langle \psi' J' \left\| U^{(\lambda)} \right\| \psi J \right\rangle^2 F \tag{27}$$

$$W_{d-m} = \frac{S_L}{(2J+1)G} \frac{2\pi e^2}{\hbar} \sum_{\lambda} (\lambda + 1) \frac{\left\langle r^{\lambda} \right\rangle^2}{\left(R_L^{\lambda+2}\right)^2} \times \left\langle f \left\| C^{(\lambda)} \right\| f \right\rangle^2 \left(1 - \sigma_{\lambda}\right)^2 \left\langle \psi' J' \left\| U^{(\lambda)} \right\| \psi J \right\rangle^2 F$$
(28)

$$W_{ex} = \frac{(1 - \sigma_0)^2}{(2J + 1)G} \frac{8\pi}{\hbar} \frac{e^2}{R_L^4} \left\langle \psi' J' \| S \| \psi J \right\rangle^2 \sum_m \left| \left\langle \phi \left| \sum_j \mu_z(j) s_m(j) \right| \phi^* \right\rangle \right|^2 F$$
(29)

where R_L is the donor–acceptor states distance, Ω_{λ}^{FED} are the intensity parameters (or Judd-Ofelt parameters) by the Forced Electric Dipole (FED) mechanism [46,48]. The Simple Overlap Model [41,42] was employed to calculate these quantities through the JOYSpectra web platform [35]. The values of the squared reduced matrix elements $\left\langle \psi' J' \left\| U^{(\lambda)} \right\| \psi J \right\rangle^2$ were taken from Carnall et al. [39] whereas the $\langle \psi' J' || S || \psi J \rangle^2$ matrix elements were calculated using free-ion wavefunctions in the intermediate coupling scheme [94,95]. The values of $\langle \psi' J' || S || \psi J \rangle^2$ for allowed ($| \Delta J | = 0$ or 1) ${}^7F_0 \to {}^5D_1$, ${}^7F_1 \to {}^5D_0$, ${}^7F_1 \to {}^5D_0$ 5D_1 , $^7F_1 \rightarrow ^5D_2$, and $^7F_1 \rightarrow ^5G_2$ acceptor transitions were reported in [96]. S_L is the dipole strength of the ligand transition involved in IET (10^{-36} and 10^{-40} esu² cm² for S_1 and T_1 , respectively [9]), $\langle r^{\lambda} \rangle$ are the 4f radial integrals [97], G is the ligand state degeneracy (G = 1 or 3 for S_1 or T_1 , respectively), $\left\langle f \left\| C^{(\lambda)} \right\| f \right\rangle$ is the reduced matrix element of Racah's tensor operators [98], and $(1 - \sigma_{\lambda})$ (for $\lambda = 1$ and 2) are the shielding factors which have a relation with the overlap integrals between valence orbitals of the pair Ln-X (X as the ligating atom in the first coordination sphere) [57,93]. The values of $(1 - \sigma_{\lambda})$ for $\lambda = 4$ and 6 can be found in Ref. [97]. s_m (in Eq. (3)) is the spin operator in the ligand and μ_z is the dipole operator (z-component), the value of the matrix element of these coupled operators is 10^{-36} (esu)² cm² [9,99].

The F term in Eqs. (27)–(29) is the density of states (proportional to the spectral overlap) that considers the energy mismatch condition between donor (ligands) and acceptor (Ln(III) ion) states [9,90]. F can be estimated by:

$$F = \frac{1}{\hbar \gamma_D} \sqrt{\frac{\ln(2)}{\pi}} e^{-\left(\frac{\Delta}{\hbar \gamma_D}\right)^2 \ln(2)}$$
(30)

where Δ is the energy difference between the donor barycenter state and the lanthanide ion acceptor state ($\Delta = E_D - E_A$). γ_D is the bandwidth at half-height of the donor states (S1 and T1), assumed here to have a typical value of $\gamma_D = 3000 \text{ cm}^{-1}$ for both 1 and T₁ states [100,101]. The donor-acceptor distance (R_L in Eqs. (27)-(29)) is a fundamental quantity to evaluate the IET rates and is traditionally calculated as follows [9,91]

$$R_{L} = \frac{\sum_{i} c_{i}^{2} R_{L}(i)}{\sum_{i} c_{i}^{2}} \tag{31}$$

where c_i is the *i*th atomic orbital coefficient contributing to the ligand donor states (S₁ or T₁) and $R_L(i)$ is the distance between c_i atomic center and the Ln(III) ion. Although R_L calculated from Eq. (31) was successfully applied several times, this formulation does not consider the weights of molecular orbital compositions constituting the donor state, and only the main MO excitation (or a non-weighted average) is considered in the calculation. Table 1 exemplifies a triplet state calculated from TD-DFT (see the Supporting Information file of Ref. [102]).

This triplet state (Table 1) has contributions from molecular orbitals with index 306, 307, 308, and 309. Thus, R_L is obtained from the atoms

Table 1
Illustrative example of a triplet excited state composition, highlighting each molecular orbital (and its weight) involved in each excitation that composes the state.

Excited state 1	Triplet-A (26843 cm ⁻¹)
301 → 306	0.10033
301 → 307	0.15672
301 → 308	0.61833
301 → 309	0.12884

involved in these molecular orbitals. However, MO weights (numbers on second column) are not taken into account. Here is proposed an expression for R_L considering each MO excitation weight as follows:

$$R_{L} = \frac{\sum_{i,j} a_{j}^{2} c_{i}^{2} R_{L}(i)}{\sum_{i,j} a_{i}^{2} c_{i}^{2}}$$
 (32)

where a_j is the contribution of the jth orbital excitation that composes the excited state. This reformulation allows for a better R_L description of donor state electronic density barycenter.

The forward energy transfer rates (*W*) are calculated by summing up Eqs. (27)–(29) for same pathway (e.g., $T_1 \rightarrow [^7F_0 \rightarrow ^5D_1]$):

$$W = W_{d-d} + W_{d-m} + W_{ex} (33)$$

If Δ in Eq. (30) is negative, W must be multiplied by the energy barrier $e^{(\Delta/(k_BT))}$, where k_B is the Boltzmann constant and T is the temperature (considered 300 K in the present work). Also, depending on the Eu(III) initial state involved in the energy transfer pathway (e.g., 7F_1 in $T_1 \rightarrow [{}^7F_1 \rightarrow {}^5D_1]$ pathway or 7F_0 in $S_1 \rightarrow [{}^7F_0 \rightarrow {}^5L_6]$ pathway), W is multiplied by the thermal population fraction at room temperature (approximately 0.64 for 7F_0 and 0.33 for 7F_1) [95,103].

The IET rates from the ligands to the Eu(III) ion are calculated using both $S_1 \rightarrow S_0$ and $T_1 \rightarrow S_0$ decays as energy donors localized in the ligands and, by selection rules on J quantum number, a total of 32 energy transfer pathways involving 7F_0 and 7F_1 as initial states and 5D_0 , 5D_1 , 5D_2 , 5D_3 , 5L_6 , 5L_7 , 5G_2 , 5G_3 , 5G_6 , 5D_4 , and 5G_5 as final states at the Eu(III) ion. Therefore, considering also the backward energy transfer (Ln(III) \rightarrow Ligand), a total of 64 IET pathways are calculated for each studied complex on the JOYSpectra web platform [35].

2.6. Rate equations and overall emission quantum yield

When all IET rates are determined, the system of rate equations constituted by coupled ordinary differential equations (ODEs) can be solved to determine the relative population of each level. In this work, the set of ODEs was solved through time propagation using the Radau method [104]. The set of coupled ODEs can be described as follows [8, 9.105]

$$\frac{d}{dt}P_i(t) = \sum_{j=1} W_{j\to i}P_j(t) - \sum_{j=1} W_{i\to j}P_i(t), \quad \text{with } i \neq j$$
(34)

where both summations span all levels of the system. P_i and P_j are the populations of the levels $|i\rangle$ and $|j\rangle$, $W_{j\rightarrow i}$ and $W_{i\rightarrow j}$ are the energy transfer rates between these states. Thus, a N-level rate equations model can be described by a set formed by N coupled ODEs. As mentioned before, we adopted the Radau method [104] in the simulations since it has been successfully applied in other Ln-based complexes and provided reliable results [8,96,102,106–109] with a low computational cost. Each simulation was done in a time interval from 0 to 50 ms with a step-size of 2 μ s.

The solution of the rate equations model allows the estimation of the ${}^5\mathrm{D}_0$ emitting level population (P_E) and the emission intensity $I = A_{rad}P_E$, where A_{rad} is the spontaneous emission coefficients which can be calculated from the Judd–Ofelt intensity parameters [9,11,35,39,46,48]. The A_{rad} values were also obtained from the JOYSpectra program.

The overall quantum yield Φ_{ovl} is defined by the ratio of the numbers of photons emitted and absorbed by the complex [9,10,110,111],

$$\Phi_{ovl} = \frac{\text{number of photons emitted}}{\text{number of photons absorbed}} = \frac{A_{\text{rad}} P_E}{\phi P_0}$$
 (35)

where P_0 is the population of the ground level and $\phi = \sigma \rho \lambda_{exc}/hc$ is the pumping rate of the populations from this level (e.g. $S_0 \rightarrow S_1$ intra-ligand absorptions), where σ is the absorption cross-section of the ligand (in the order of ca. 10^{-16} cm² molecule⁻¹ [112]), ρ is the power density in units of W cm⁻², λ_{exc} is the excitation wavelength, h is Planck's constant and c the speed of light [8,102,106,113].

2.7. Computational procedures

A comprehensive assessment of different initial conformations was performed using RM1/Sparkle [114], implemented on MOPAC 2016 [115], for the $[Eu(L)Cl(H_2O)_3]$ (with L = L2 and L5) coordination compounds. The most stable geometries were used in the next steps. All geometry optimizations and subsequent normal vibrational frequency calculations were performed with Gaussian 16 [88], utilizing an ultrafine integration grid [116] and a tight convergence criterion for the SCF procedure. The ω B97X-D functional [117] was utilized with the Def2-TZVP [118] basis set to describe all ligand atoms and MWB52 pseudo-potential [119] and valence electrons basis set for the Eu(III) ion. No geometrical constraints were imposed on the complex under study. The excited states (T₁ and S₁) were obtained employing the timedependent DFT approach (TD-DFT) [120] at the same level of theory described for the geometry optimizations (ωB97X-D/MWB52(Eu)/Def2-TZVP). Local mode analysis (LMA) was performed with the standalone LModeA package [38] with local mode parameters generated with a development version for large systems. Occupied Localized Molecular Orbitals were calculated using Pipek-Mezey [121] based on Becke population [122] implemented in the Multiwfn package [89].

Fig. 3 illustrates the general computational protocol featured in this work for the obtention of underlying Ln–L properties, which can be outlined as:

- Equilibrium geometries and normal vibrational frequencies calculated at the DFT level (or other methods).
- From equilibrium geometries: Bond distances R_j are used in Eqs.
 (4) and (5).
- From normal vibrational frequency calculations, local vibrational mode properties are calculated using Eqs. (18)-(21); each normal mode is decomposed into local mode contributions using Eqs. (23)-(26). Local mode force constants k_n^a are obtained.
- Local mode force constants k^a_n are used in Eq. (7) to calculate charge factor g and both are used in Eq. (4).
- From R_j , type of ligand atom, and parameters from Ref. [57]: ρ , β , and α_{OP} are used in Eqs. (4) and (5).
- T₁ and S₁ excited states energies and compositions: Donor-acceptor energy differences Δ and R_L are used in Eqs. (27)–(30) and (32).
- Localized Molecular Orbitals: α' calculated based on Algorithm 1 and used in Eq. (5).

3. Results and discussion

Tables 2–4 summarize the results obtained for systems $[Eu(L2)Cl(H_2O)_3]$ and $[Eu(L5)Cl(H_2O)_3]$ and is discussed in three subsections. In Section 3.1, Ln–L bond properties are discussed regarding relationships between k^a , R, α_{OP} , and α' . CNM results for normal vibrational modes associated with the Ln–L bonds are examined as well. In addition, theoretical intensity parameters are presented in line with experimental data. In Section 3.2, the excited states properties and energy transfer rates obtained with the featured methodologies are discussed. In Section 3.3, rate equations involving the energy transfer mechanisms are discussed and shown to explain the theoretical overall quantum yield and its agreement with experimental data.

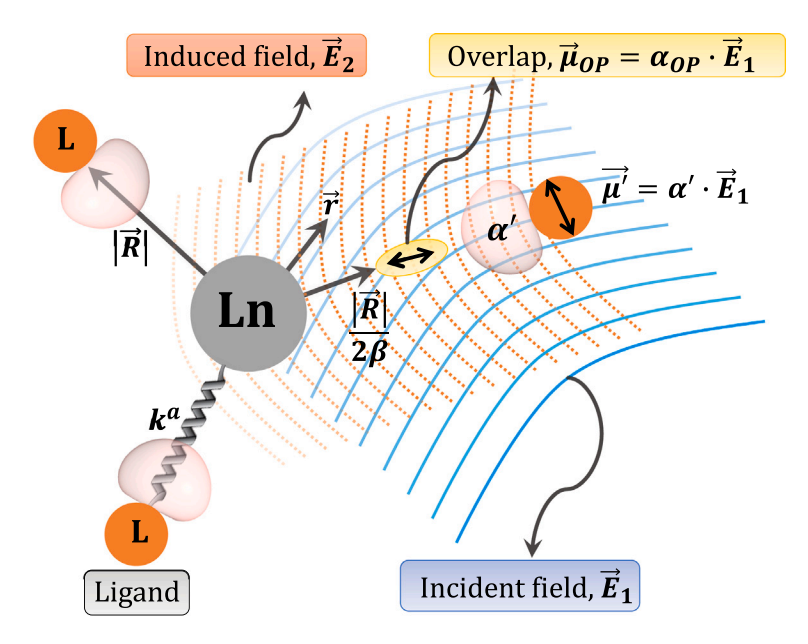


Fig. 3. Illustrative description of the computational modeling utilized in BOM (DC) and SOM (FED). $|\vec{R}|$ and k represent the Ln(III)-ligating atom distance and its chemical bond force constant, respectively. α' is the ligand effective polarizability while α_{OP} is the overlap polarizability of the Ln(III)-ligating atom chemical bond.

Table 2 Calculated Eu–L bond properties: Bond distance R (in Å), local force constant k^a (in mdyn/Å), charge factor g (dimensionless), overlap polarizability (in 10^{-2} Å 3), and ligand effective polarizability (in Å 3).

Bond	[Eu(L2)Cl(H ₂ O) ₃]				[Eu(L5)Cl(H ₂ O) ₃]					
Property	R	k^a	g	α_{OP}	α'	R	k^a	g	α_{OP}	α'
Eu1-N2	2.58	0.85	2.27	2.35	1.04	2.59	0.88	2.32	2.31	1.01
Eu1-N4	2.58	0.85	2.27	2.38	1.13	2.59	0.87	2.31	2.30	1.01
Eu1-O5	2.52	0.63	1.67	2.96	1.22	2.52	0.63	1.67	2.97	1.23
Eu1-O6	2.54	0.56	1.59	2.87	1.13	2.54	0.57	1.60	2.84	1.13
Eu1-O9	2.54	0.56	1.59	2.85	1.14	2.54	0.56	1.59	2.84	1.13
Eu1-S3	2.88	0.57	1.91	4.10	2.52	2.87	0.61	1.96	4.13	2.60
Eu1-S8	2.87	0.62	1.99	4.14	2.54	2.87	0.59	1.94	4.12	2.58
Eu1-Cl7	2.73	0.76	2.03	3.62	1.38	2.73	0.75	2.01	3.62	1.32

3.1. Ln-L bond properties and theoretical intensity parameters

Despite the fact that the equilibrium geometries obtained for both compounds are in a conformation under C₁ point group, the coordination polyhedron (that includes all Ln–L bonds) is close to C_S and exhibit equivalent bonds with similar properties, as seen in Table 2. Such similarity is illustrated in Fig. 4, which shows LMOs assigned to chemical groups responsible for ligand-Ln coordination and their corresponding effective polarizabilities (α' in Fig. 4). The results obtained for α_{OP} are in the same order of magnitude as that found for β -diketonate [21,56, 85] ligands, and are observed to follow the trend $\alpha_{OP}(\text{Eu-S}) > \alpha_{OP}(\text{Eu-S})$ Cl) > $\alpha_{OP}(\text{Eu-O})$ > $\alpha_{OP}(\text{Eu-N})$, the same trend as observed for α' . Both overlap and ligand effective polarizabilities are associated with the bond electron density ability to be distorted by an external electric field. Atomic and molecular polarizabilities generally increase as the volume occupied by electrons increases. However, α_{OP} and α' localized nature reflects the behavior of atoms or groups within molecules, as already reported [21]. In that sense, S-C fragments in mercapto-triazole and Cl- anion are expected to have greater polarizabilities than that of neutral ligands (e.g., H2O), or molecular electronegative fragments such as sp² NNC.

The Eu1–N2 and Eu1–N4 bonds are almost equivalent for both systems, and the same similarity is observed for the Eu1–S3 and Eu1–S8 bonds. Eu1–O6 and Eu1–O9 are equivalent bonds involving $\rm H_2O$ ligands with $\rm Cl^-$ as neighbor and has similar calculated properties. The third $\rm H_2O$ ligand forms a Eu1–O5 bond which is non-equivalent to the other two Eu–O. It is noteworthy that unlike the other Eu–L bonds in the studied systems, $\alpha'(\rm Eu-O)$ values involve all LMOs (2

O–H bonds and 2 O lone-pairs) localized on the H_2O molecule. Fileti and coworkers calculated (MP2/aug-cc-pVDZ) [123] the isolated H_2O molecule polarizability as having the value of 1.376 ų, while the experimental value is 1.450 ų [124]. For the Cl⁻ anion, calculated α' is also the total polarizability for the atomic fragment. Isolated Cl⁻ anion calculated (MP2/aug-cc-pVDZ) and experimental atomic polarizabilities are 3.37 and 3.94 ų, respectively [125]. It is remarkable that the α' values reported here for these atomic (Cl⁻ anion) and molecular (H_2O) fragments are below the isolated counterparts polarizabilities values, indicating a less intense induced dipole with the applied field for these fragments, which depends on local connectivity [126]. The results reported here are in line with the following trend: the fragment electron densities (including the lone-pairs), when interacting with Eu(III) cation, become less polarizable than their isolated counterparts.

Fig. 5 depicts the comparison between local force constants k^a and R, α_{OP} , and α' values, revealing important trends. Distance R and k^a values for the Eu–N, Eu–S, and Eu–Cl bonds in the studied systems (see Table 2 and Fig. 5a) are qualitatively connected via a generalized Badger rule relationship [129,130]. k^a values for Eu–O bonds involving H₂O ligands do not follow the same relationship with R found in Eu–L (with L = N, S, and Cl). It should be mentioned that the shorter bond is not always the stronger bond, as reported in the literature [131,132]. Our results show that H₂O, being neutral ancillary ligands, exhibit weaker Eu–O bonds among Eu–L ones (with L = O, N, S, and Cl), despite presenting small bond distances.

Fig. 5b depicts a comparison between k^a and α' values with a linear relationship for Eu–L (with L = N, S, and Cl). It is observed that stronger bonds (Eu–N with highest k^a values) exhibit smaller α' values,

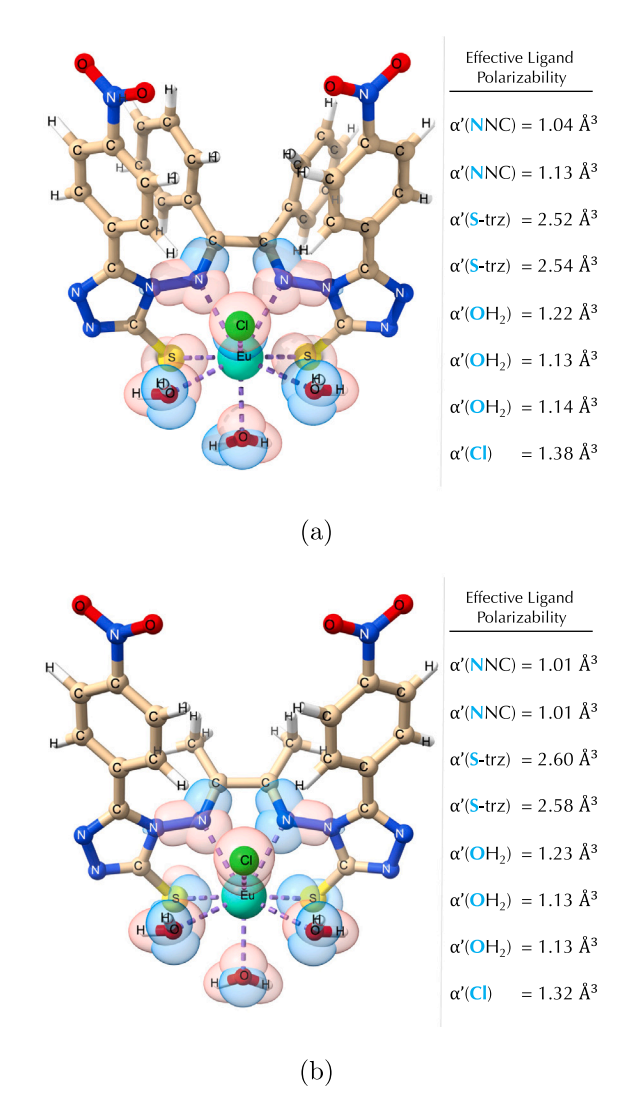


Fig. 4. Localized Molecular Orbitals utilized in the ligand effective polarizability calculations for (a) $[Eu(L2)Cl(H_2O)_3]$ and (b) $[Eu(L5)Cl(H_2O)_3]$ compounds. Rendering of LMOs were made on the ChimeraX software [127,128] with isosurfaces of 0.15 e/a_0^3 .

in line with the Badger type k^a versus R behavior. Higher k^a values are associated with small distances, which in turn is reflected on less polarizable lone-pair electron densities.

Here is noteworthy to mention that atoms (or chemical fragments) that hold on their electrons tightly are less polarizable [133]. On the other hand, molecules with higher permanent dipoles are less likely to change shape due to an external electric field, being also less polarizable. Water is a very small polar molecule and exhibits small molecular polarizability due to its large permanent dipole moment. For the sake of comparison, reference values [134] for molecular dipoles (in Debye — D) and polarizabilities (in ų) make this trend clear. While dipole moments vary in increasing order H_2S (0.98 D) < HCl (1.09 D) < NH₃ (1.48 D) < H_2O (1.88 D), molecular polarizabilities vary in decreasing order H_2S (3.63 ų) > HCl (2.50 ų) > NH₃ (2.10 ų) > H_2O (1.50 ų).

Another aspect is that ligands in Ln(III) complex are acting as Lewis bases. When a ligand approach the Eu(III) ion, a permanent density polarization is induced by +3 lanthanide charge. Bakó and coworkers reported the increase of polar molecules (including water) permanent dipole when interacting with cations [135]. In this regard, stronger Ln–L interactions lead to more polarized and, as a consequence, less polarizable chemical environment. This trend is in line with the results

Table 3 Calculated experimental and theoretical intensity parameters (in $10^{-20}\ cm^2$) for the studied compounds.

Ω_{λ}	$[Eu(L2)Cl(H_2O)_3]$	[Eu(L5)Cl(H ₂ O) ₃]
Ω_{2}^{exp}	9.98	9.84
$rac{arOmega_2^{exp}}{arOmega_4^{exp}}$	5.64	5.56
Ω_{2}^{theo}	7.14	8.42
$arOmega_4^{ ilde{theo}}$	4.07	3.91
Ω_6^{iheo}	1.28	1.30

^aExperimental intensity parameters calculated using Eq. (1) and Fig. 2.

reported here. The $\mathrm{H}_2\mathrm{O}$ ligands are an exception for this trend probably as a consequence of their already high permanent dipole, which is not much affected by the coordination with Eu(III). This can be seen when their isolated polarizability (ca. 1.4–1.5 ų) is compared with obtained α' values (ca. 1.1–1.25 ų). α_{OP} values follow similar trend with k^a (see Fig. 5c) as observed for α' , which is expected given that $\alpha_{OP} + \alpha'$ represents the chemical environment polarization capability experienced by the Eu(III) ion.

We used in this work as an assessment tool the characterization of normal mode (CNM) procedure, which is an integral part of the local mode analysis (LMA) [34,58,60–62]. CNM decomposes normal vibrational modes into local mode contributions and has led to a new way of analyzing vibrational spectra, as successfully shown by recent applications such as the investigation of pKa probes [136] and to gain insights into *vibrational Stark effect* probes [84]. Herein our results cover all normal vibrational modes within the frequency range that captures the innermost stretching vibrations of the Eu(L2)Cl(H2O)3 and Eu(L5)Cl(H2O)3 complexes. Local mode parameters are indicated by chemical symbols followed by the index number of the atoms according to the specification given in the sketches embedded in Fig. 6. Two, three or four atomic symbol abbreviations mean, respectively, bond stretching, bond angle, and dihedral angle local mode parameters.

According to experimental data [33], the infrared spectral region of ca. $420-340 \text{ cm}^{-1}$ for the $[Eu(L2)Cl(H_2O)_3]$ and $[Eu(L5)Cl(H_2O)_3]$ complexes features Ln-S and Ln-N stretching vibrations. Fig. 6 shows that such characteristic stretching vibrations can be probed via CNM in the computed frequency range of ca. 120–280 cm $^{-1}$. The vibrational coupling between the local vibrational modes involving Eu(III), as well as the degree of delocalization of the normal vibrational modes, are revealed on a quantitative basis. O5Eu1 is responsible for the greatest local mode character of the normal vibrational mode at 277 cm⁻¹ for both Eu(L2)Cl(H₂O)₃ (51%) and Eu(L5)Cl(H₂O)₃ (56%). All of this represents an advance towards a deeper understanding of the spectral region featuring the characteristic vibrations of Ln-containing complexes, a finding which could also be utilized to monitor structural changes with emphasis on photochemical processes. CNM plots clarify the importance of LMA in the context of Ln(III) local chemical environment description by showing that each normal mode in the frequency range attributed to Ln-L interactions couples different molecular fragments movements. These results reveal the impossibility of utilizing normal modes for the desired description of force constants within the SOM scope (Eq. (7)), featuring local force constants as the proper descriptor.

Using Eq. (19) to obtain k^a and Eq. (7) to calculate charge factors g that appear in Eq. (4) makes it possible to calculate the theoretical intensity parameters ($\Omega_{\lambda}^{\text{theo}}$) by using Eq. (3). It is noteworthy that the proper description of local force constants (through g) in Eq. (4) leads to a better description of energy transfer rate equation through dipole-dipole mechanism (Eq. (27)) and consequently the total W (Eq. (33)). Table 3 reveal a very good agreement between the obtained values for experimental and theoretical intensity parameters, considering that methodologies and tools commonly available in literature for $\Omega_{\lambda}^{\text{theo}}$ calculations involve some level of fitting procedure [9].

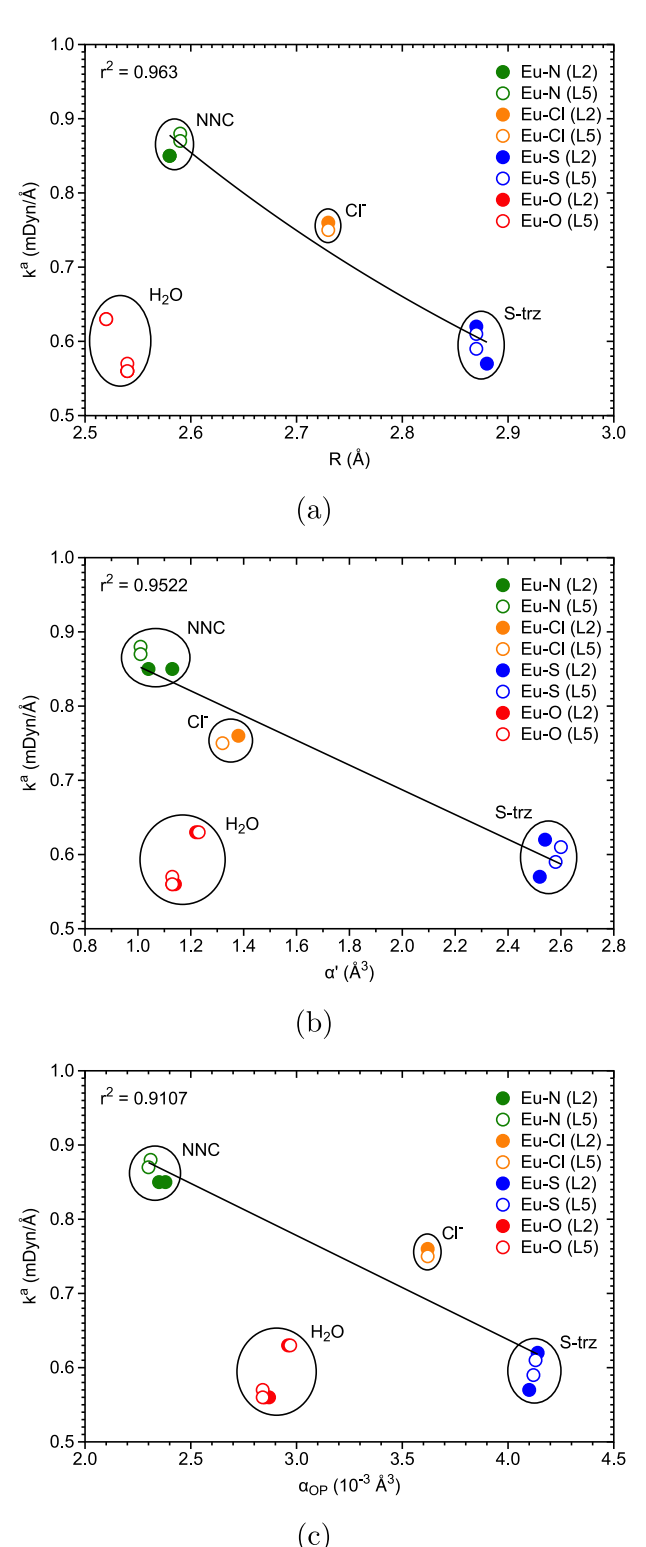


Fig. 5. Local stretching force constant k^a (in mDyn/Å) *versus* (a) Eu–L bond distance R (in Å); (b) effective ligand polarizability α' (in ų); and (c) overlap polarizability α_{OP} (in 10^{-3} Å). Different bonds are separated by colors; the Eu–O(H₂) outliers are highlighted by red circles. The red circles of L2 are fully hidden by those of L5 in (a). (For interpretation of the references to color in this figure legend, the reader is referred to the web version of this article.)

Table 4 Singlet (S_1) and triplet (T_1) first excited states properties obtained for the studied compounds: Energies E (in cm⁻¹) and donor–acceptor distances R_L (in Å); forward $(W^S$ and W^T) and backward $(W_b^S$ and W_b^T) IET rates (in s⁻¹); and theoretical overall quantum yields $(Q_{L_B}^I$ in %).

State		[Eu(L2)Cl(H ₂ O) ₃]	[Eu(L5)Cl(H ₂ O) ₃]
	E	35587	35211
S_1	R_L	6.64	6.33
	W^S	1.05×10^{4}	2.29×10^{4}
	W_b^S	1.01×10^{-15}	1.24×10^{-14}
T ₁	E	18182	19455
	R_L	4.52	3.99
	W^{Ta}	4.74×10^{6}	1.13×10^{9}
	W_b^{Ta}	1.22×10^{8}	1.18×10^{8}
	$W^{T'b}$	7.65×10^7	2.45×10^{8}
	$W_b^{T'}$ b	3.15×10^{6}	2.16×10^4
	Φ_{ovl}	48.77 (50) ^c	55.72 (53) ^c

^aAll IET pathways excluding ⁵D₀.

3.2. Excited states and energy transfer

Table 4 summarizes the singlet (S_1) and triplet (T_1) first excited states properties obtained for the studied compounds. Forward and backward IET rates (from Eq. (33)) are also shown. S_1 and T_1 molecular orbitals compositions are illustrated in Figs. 7 and 8, from which it can be noticed that the S_1 state for both complexes is more spread out in the molecule, leading to higher R_L (6.64 and 6.33 Å) values. On the other hand, T_1 states exhibit shorter R_L as a consequence of higher weights $(a_i$ in Eq. (32)) associated with shorter $R_L(i)$.

For the sake of comparison between R_L obtained with Eqs. (Eq. (31)) and (Eq. (32)), R_L with traditional equation (Eq. (31)) would lead to much different values, namely, for $[Eu(L2)Cl(H_2O)_3]$ $R_I(S_1) =$ 4.09 Å, $R_I(T_1) = 3.04$ Å; and for $[Eu(L5)Cl(H_2O)_3]$ $R_I(S_1) = 3.48$ Å, $R_L(T_1) = 3.87$ Å. These differences may lead to dramatic changes in the IET rates and, consequently, in overall quantum yield, as it will be shown in Section 3.3. The values of R_L obtained from Eq. (31) (Table S2) are, with no exception, shorter than the ones obtained from Eq. (32) and this leads to higher IET rates. As a consequence, the calculated overall quantum yield can be overestimated, as observed for $[Eu(L5)Cl(H_2O)_3]$ in which the $S_1 \rightarrow Eu(III)$ starts populating Eu(III)upper levels and, therefore, increasing ⁵D₀ population (see Table **S2**). Even with shorter donor-acceptor distances, this overestimation in Q_{In}^{L} is not clearly observed for the [Eu(L2)Cl(H2O)3] complex because the ISC rate of $S_1 \rightarrow Eu(III)$ is ten times smaller than that of $S_0 \rightarrow T_1$, making $S_0 \rightarrow T_1 \rightarrow Eu(III)$ as the dominant channel to feed the Eu(III)

 S_1 and T_1 first excited states energies are in line with values found for a complex with similar type of ligands [137], with $\Delta E_{S_1-T_1} \approx 15000~{\rm cm}^{-1}$, which influences the overall quantum yield. The complete data for forward (W^S and W^T) and backward (W^S_b and W^T_b) IET rates, including the W_{d-d} , W_{d-m} , and W_{ex} mechanisms contributions (Eqs. (27)–(29)), are presented in Tables S3 and S4. These data were obtained considering the S_1 and S_1 energies and donor–acceptor distances (S_1) in Table 4.

Fig. 9 shows energy levels diagram that illustrates the ligand-to-Eu(III) energy transfer process. A total of 128 IET rates (64 for each complex, of which 32 for the forward and 32 for backward energy transfer) were obtained with non-zero contributions (see Tables S3 and S4), where pathways from 1 to 16 represent the contributions from S_1 and pathways from 17 to 32 represent the T_1 contributions. W^S and W^T are the sum over all forward pathways (ligand-to-Eu(III)) while W^S_b and W^T_b are the rates for the backward ones (Eu(III)-to-ligand) (as summarized in Table 4).

^bOnly considering IET pathways to ⁵D₀.

^cExperimental values from Ref. [33].

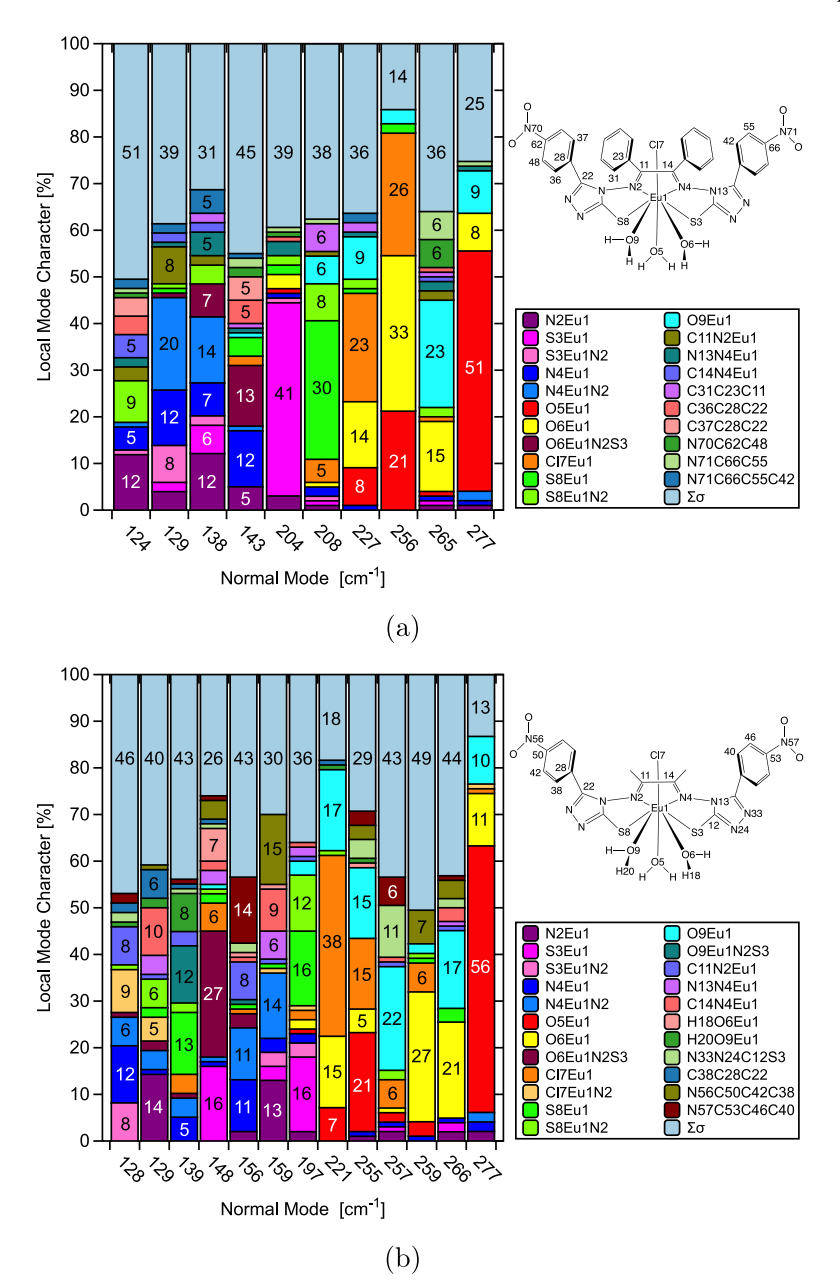


Fig. 6. CNM plots of the characteristic vibrational region of (a) $Eu(L2)Cl(H_2O)_3$ and (b) $Eu(L5)Cl(H_2O)_3$ at the ωB97X-D/(MWB52)Def2-TZVP level of theory (see text for details). Σσ comprises the summation of all of the σ local mode contributions below the threshold of 5%.

IET results indicate $T_1 \to Eu(III)$ as the most effective energy transfer channel for both complexes. For $[Eu(L2)Cl(H_2O)_3]$ and $[Eu(L5)Cl(H_2O)_3]$ complexes, pathway 13 involving S_1 (from S_1 to $^7F_1 \to ^5G_2$) has the highest forward IET rate. From T_1 donor, pathways 17 (from T_1 to $^7F_0 \to ^5D_1$) and 32 (from T_1 to $^7F_1 \to ^5D_0$) are the main contributions for W^T and $W^{T'}$ rates, respectively. It is significant that all pathways mentioned before are dominated by the exchange mechanism (W_{ex} , Eq. (29)).

3.3. Rate equations and overall quantum yield

Based on schematic energy level diagrams in Fig. 9, the population kinetics can be described by the general rate equations model given in Eq. (36) for all complexes.

$$|\mathbf{0}\rangle$$
: $\frac{d}{dt}P_0 = -\phi P_0 + \frac{1}{\tau_T}P_1 + \frac{1}{\tau_S}P_2 + W_g P_5$ (36a)

$$|1\rangle: \frac{d}{dt}P_1 = -\left(\frac{1}{\tau_T} + W^T + W^{T'}\right)P_1 + W_{ISC}P_2 + W_b^T P_3 + W_b^{T'} P_4$$
(36b)

$$|2\rangle$$
: $\frac{d}{dt}P_2 = -\left(\frac{1}{\tau_S} + W^S + W_{ISC}\right)P_2 + W_b^S P_3 + \phi P_0$ (36c)

$$|3\rangle$$
: $\frac{d}{dt}P_3 = -(W_b^S + W_b^T + W_{3\rightarrow 4})P_3 + W^S P_2 + W^T P_1$ (36d)

$$|4\rangle: \frac{d}{dt}P_4 = -\left(\frac{1}{\tau} + W_b^{T'}\right)P_4 + W^{T'}P_1 + W_{3\to 4}P_3$$
 (36e)

$$|5\rangle$$
: $\frac{d}{dt}P_5 = -W_gP_5 + \frac{1}{\tau}P_4$ (36f)

with P_N representing the population of the $|{\rm N}\rangle$ level as depicted in Fig. 9. τ_S , τ_T , and τ are the decay lifetimes of the S₁, T₁, and $^5{\rm D}_0$ levels. Typical values of these quantities for Ln-based complexes range from 10^{-9} to 10^{-6} s for τ_S , 10^{-6} to 10^{-3} s for τ_T , and 10^{-3} s for τ [9,102,107]. W_{ISC} is the S₁ \rightarrow T₁ intersystem crossing rate which is in the order of 10^7 s⁻¹ for the energy gap between S₁ and T₁ of $\Delta E_{\rm ST} \approx$

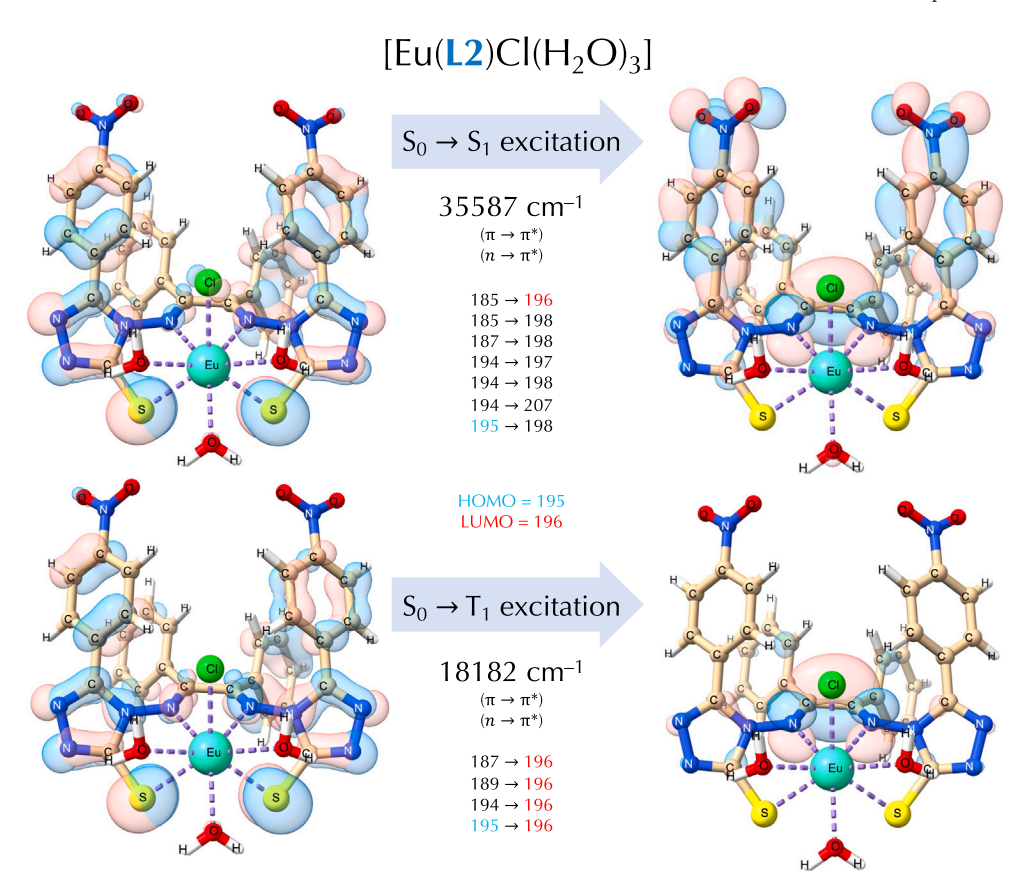


Fig. 7. Monoelectronic states involved in the absorption spectrum singlet–singlet and singlet–triplet excitations for the $[Eu(L2)Cl(H_2O)_3]$ complex calculated using ω B97X-D/(MWB52)def2-TZVP level in TD-DFT theory. Excitation energies, main MO transition indexes (with composition percentages from a_j^2 in Eq. (32)) in each excitation, and HOMO and LUMO index are indicated. Rendering of molecular orbitals were made on ChimeraX software [127,128] with isosurfaces of 0.04 e/a_0^3 .

15000 cm⁻¹ [102], which is the case of the studied complexes. Once we are treating the ligand levels separated from the 4f levels of the Eu(III) in an independent system model, W_g (set to 10^{10} s⁻¹) is the rate from the 7F_J to S_0 to avoid the concentration of the molecular population in the Eu(III) ground level. This is necessary because, fundamentally, a molecular system has only one ground state which should be described as $|S_0, \, ^7F_0\rangle$.

To obtain estimations of the Eu(III) $^5\mathrm{D}_0$ emitting level population, $^5\mathrm{D}_0$ (state $|4\rangle$ in Eq. (36)e and Fig. 9) was separated from the Eu(III) upper levels (state $|3\rangle$ in Eq. (36)d and Fig. 9). Thus, the quantities $W_b^{T'}$ and $W^{T'}$ represent the backward energy transfer rates involving only the Eu(III) emitting level $^5\mathrm{D}_0$ and they are obtained by the sum of pathways 31 and 32 in Tables S3 and S4.

The population simulations using Eq. (36) consider the boundary conditions which guarantee that the sum of the populations over all energy levels should be constant at any time t [109,138]. Thus, the following relationship must be preserved:

$$\sum_{N} P_N(t) = 1 \tag{37}$$

where $P_N(t)$ is the population of state N at time t with $0 \le t \le t_f$. Since all compounds present T_1 above the 5D_0 level, the values of $W_b^{T'}$ (energy transfer from 5D_0 to T_1) are very low and can be neglected. On the other hand, the T_1 lower energy position provided high values of $W^{T'}$ (energy transfer rates from T_1 to 5D_0 level).

The theoretical overall quantum yield for both complexes (see Table 4) are in very good agreement with experimental data, specially considering that no fitting procedures were adopted to describe theoretical intensity parameters. Theoretical overall quantum yield calculated with original R_L formulation ($\Phi_{ovl}=55.72\%$) is less accurate than the new formulation counterpart ($\Phi_{ovl}=66.00\%$) when compared against

experimental data ($\Phi_{ovl}=53\%$). Different R_L values affect the overall quantum yield by changing the effectiveness of IET rates, as they appear as R_L^6 , $(R_L^{\lambda+2})^2$, and R_L^4 in Eqs. (27), (28), and (29), respectively.

4. Conclusions

The featured new methodologies were shown to provide modeling improvements in calculating g (through k^a) and α' for the selected systems, but the applicability of the general procedures can be extended to various other molecular systems. Theoretical Judd-Ofelt intensity parameters were calculated without fitting procedures or introducing phenomenological data, as commonly found in the literature. The local vibrational mode theory provided new insights into chemical bond analysis for Ln-based compounds. Local force constants k^a were detected to be qualitatively connected to Ln-L distances by a Badger type rule. For the first time, by measuring the Ln-L bond strength (via k^a) it was possible to unravel the chemical meaning of effective ligand polarizabilities and their relationship with k^a . The CNM procedure led to a convenient way of analyzing the infrared spectral region assigned to Ln-L vibrations, indicating a non-localized character of the associated normal vibrational modes, which confers on the local vibrational mode theory unique properties for describing Ln-L local force constants. The new donor-acceptor R_L distance formulation provided a better energy transfer kinetics description in Ln(III) based coordination compounds by including different molecular orbital transitions in the excited states.

Herein the utilization of the highlighted blend of new methodologies facilitated the achievement of more accurate overall quantum yields. The procedure featured here, without any fitting during the $\Omega_{\lambda}^{\text{theo}}$ determination, is an important milestone and opens an avenue for new improvements and benchmarks in the computational methodology for lanthanide spectroscopy.

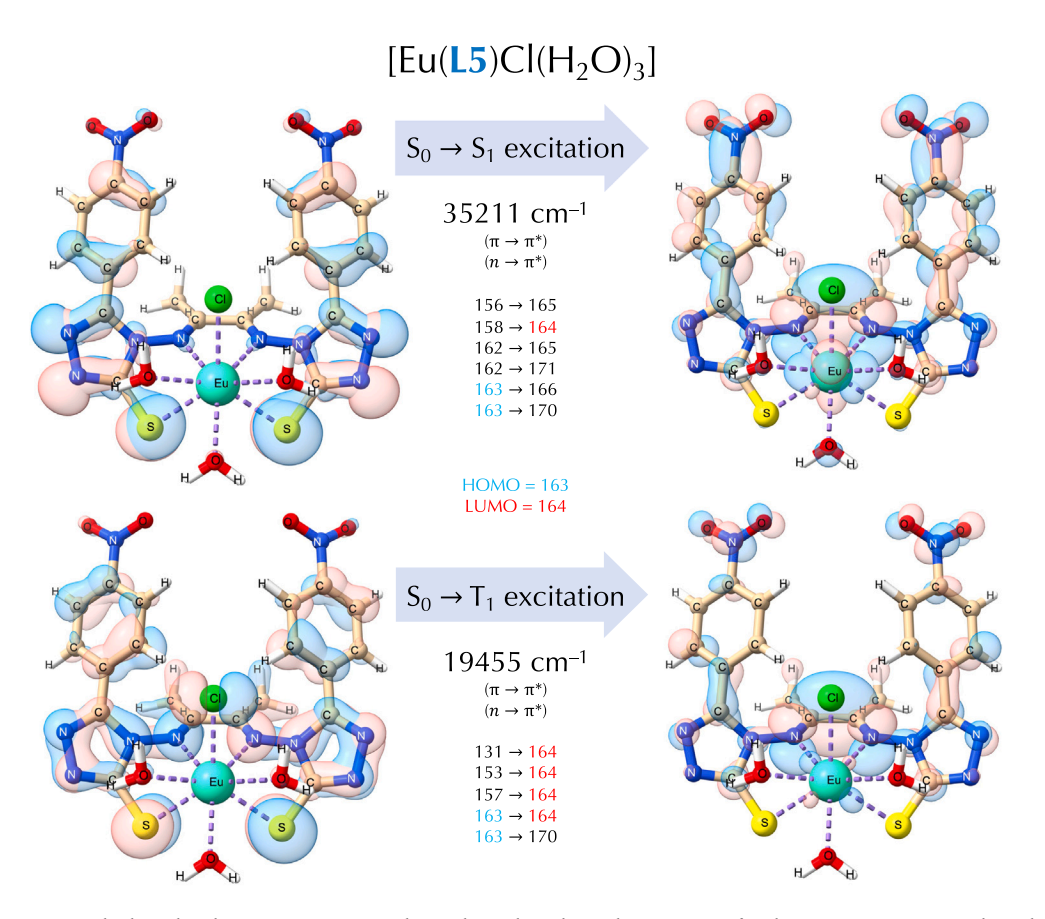


Fig. 8. Monoelectronic states involved in the absorption spectrum singlet–singlet and singlet–triplet excitations for the $[Eu(L5)Cl(H_2O)_3]$ complex calculated using $\omega B97X$ -D/(MWB52)def2-TZVP level in TD-DFT theory. Excitation energies, main MO transition indexes (with composition percentages from a_j^2 in Eq. (32)) in each excitation, and HOMO and LUMO index are indicated. Rendering of molecular orbitals were made on ChimeraX software [127,128] with isosurfaces of 0.04 e/a_0^3 .

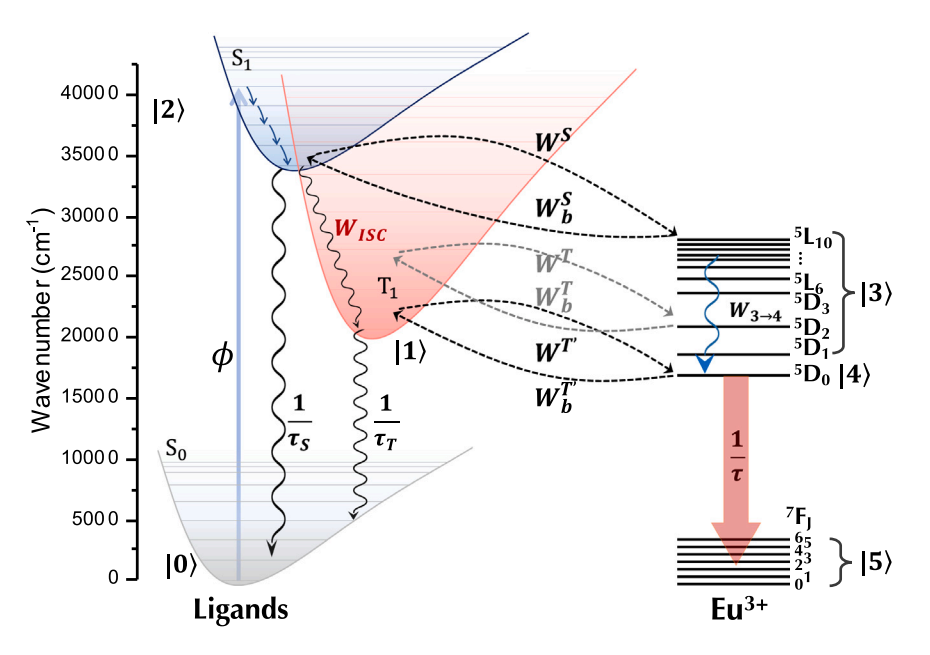


Fig. 9. Jablonski-type diagram illustrating all energy levels in the independent system model. $W^S(|2\rangle \to |3\rangle)$ and $W^T(|1\rangle \to |3\rangle)$ represent the forward IET rates from the S_1 and T_1 state, respectively. $W^{T'}(|1\rangle \to |4\rangle)$ is the forward rate from the T_1 to the Eu(III) 5D_0 emitting level. All backward IET rates are represented with a subscript b. τ_S , τ_T , and τ are the decay lifetimes from the S_1 , T_1 and T_2 0 levels, respectively. T_3 1 is the decay rate from the Eu(III) upper levels to the T_3 2 and T_4 3 absorption pumping rate.

Declaration of competing interest

The authors declare that they have no known competing financial interests or personal relationships that could have appeared to influence the work reported in this paper.

Data availability

Data will be made available on request.

Acknowledgments

We thank SMU's Center for Scientific Computing for providing generous computational resources. This work was financially supported by the National Science Foundation, Grant CHE 2102461. This work was developed within the scope of the projects CICECO-Aveiro Institute of Materials, UIDB/50011/2020, UIDP/50011/2020 & LA/P/0006/2020, and The Shape of Water (PTDC/NAN-PRO/3881/2020) financed by national funds through the FCT/MCTES (PIDDAC). M. Q. thanks SMU for the Computational Science and Engineering Graduate Fellowship.

Appendix A

All additional codes described here in addition to JOYSpectra [35] and ChemBOS [36,37] packages are available upon request. The LModeA package [38] is available upon request. For determining α' , proper usage of ChemBOS with outputs from Gaussian and Multiwfn requires the set of scripts and codes implemented in this work. Output values of α' and k^a from ChemBOS and LModeA can be directly inputted in the JOYSpectra platform.

Appendix B. Supplementary data

Supplementary material related to this article can be found online at https://doi.org/10.1016/j.omx.2022.100216. This includes experimental data, results with the original R_L , IET rates, and Cartesian coordinates for the studied complexes.

References

- U. Cho, J.K. Chen, Lanthanide-based optical probes of biological systems, Cell Chem. Biol. 27 (2020) 921–936.
- [2] C.G. Gameiro, E.F. da Silva, S. Alves, G.F. de Sá, P.A. Santa-Cruz, Lanthanide complexes dispersed in enamel: a promising new material for photonic devices, J. Alloys Compd. 323–324 (2001) 820–823.
- [3] N. Thejo Kalyani, S.J. Dhoble, Organic light emitting diodes: Energy saving lighting technology - A review, Renew. Sustain. Energy Rev. 16 (2012) 2696–2723.
- [4] A.N. Carneiro Neto, O.L. Malta, Glowing nanocrystals enable 3D X-ray imaging, Nature 590 (2021) 396–397.
- [5] X. Ou, X. Qin, B. Huang, J. Zan, Q. Wu, Z. Hong, L. Xie, H. Bian, Z. Yi, X. Chen, Y. Wu, X. Song, J. Li, Q. Chen, H. Yang, X. Liu, High-resolution X-ray luminescence extension imaging, Nature 590 (2021) 410–415.
- [6] C.D.S. Brites, A. Millán, L.D. Carlos, Chapter 281 lanthanides in luminescent thermometry, in: J.-C. Bünzli, V.K. Pecharsky (Eds.), Including Actinides, in: Handbook on the Physics and Chemistry of Rare Earths, vol. 49, Elsevier, 2016, pp. 339–427.
- [7] E.V. Salerno, A.N. Carneiro Neto, S.V. Eliseeva, M.A. Hernández-Rodríguez, J.C. Lutter, T. Lathion, J.W. Kampf, S. Petoud, L.D. Carlos, V.L. Pecoraro, Tunable optical molecular thermometers based on metallacrowns, J. Am. Chem. Soc. 144 (2022) 18259–18271.
- [8] J.F.C.B. Ramalho, A.N. Carneiro Neto, L.D. Carlos, P.S. André, R.A.S. Ferreira, Chapter 324 - Lanthanides for the new generation of optical sensing and Internet of Things, in: J.-C.G. Bünzli, V.K. Pecharsky (Eds.), Handbook on the Physics and Chemistry of Rare Earths, vol. 61, Elsevier, 2022, pp. 31–128.
- [9] A.N. Carneiro Neto, E.E.S. Teotonio, G.F. de Sá, H.F. Brito, J. Legendziewicz, L.D. Carlos, M.C.F.C. Felinto, P. Gawryszewska, R.T. Moura, R.L. Longo, W.M. Faustino, O.L. Malta, Chapter 310 Modeling intramolecular energy transfer in lanthanide chelates: A critical review and recent advances, in: J.-C.G. Bünzli, V.K. Pecharsky (Eds.), Handbook on the Physics and Chemistry of Rare Earths, Vol. 56, Elsevier, 2019, pp. 55–162.

[10] J.-C.G. Bünzli, On the design of highly luminescent lanthanide complexes, Coord. Chem. Rev. 293–294 (2015) 19–47.

- [11] H. Felinto Brito, O. Manoel Loureiro Malta, M. Claudia França Cunha Felinto, E. Epaminondas de Sousa Teotonio, Luminescence phenomena involving metal enolates, in: PATAI's Chemistry of Functional Groups, John Wiley & Sons, Ltd, 2010.
- [12] E. van Lenthe, E.J. Baerends, J.G. Snijders, Relativistic total energy using regular approximations, J. Chem. Phys. 101 (1994) 9783–9792.
- [13] E. van Lenthe, J.G. Snijders, E.J. Baerends, The zero-order regular approximation for relativistic effects: The effect of spin-orbit coupling in closed shell molecules, J. Chem. Phys. 105 (1996) 6505-6516.
- [14] M. Douglas, N.M. Kroll, Quantum electrodynamical corrections to the fine structure of helium, Ann. Phys. 82 (1974) 89–155.
- [15] B.A. Hess, Applicability of the no-pair equation with free-particle projection operators to atomic and molecular structure calculations, Phys. Rev. A 32 (1985) 756-763.
- [16] K.G. Dyall, Interfacing relativistic and nonrelativistic methods. I. Normalized elimination of the small component in the modified Dirac equation, J. Chem. Phys. 106 (1997) 9618–9626.
- [17] M.Z. Makoś, W. Zou, M. Freindorf, E. Kraka, Metal-ring interactions in actinide sandwich compounds: A combined normalized elimination of the small component and local vibrational mode study, Mol. Phys. (2020) e1768314.
- [18] D. Cremer, W. Zou, M. Filatov, Dirac-Exact Relativistic Methods: The Normalized Elimination of the Small Component Method, WIREs Comput. Mol. Sci. 4 (2014) 436-467
- [19] W. Zou, M. Filatov, D. Cremer, Analytical Energy Gradient for the Two-Component Normalized Elimination of the Small Component Method, J. Chem. Phys. 142 (2015) 214106.
- [20] B.M.T.C. Peluzo, E. Kraka, Uranium: The nuclear fuel cycle and beyond, Int. J. Mol. Sci. 23 (2022) 4655–1–4655–19.
- [21] R.T. Moura Jr., A.N. Carneiro Neto, R.L. Longo, O.L. Malta, On the calculation and interpretation of covalency in the intensity parameters of 4f-4f transitions in Eu³⁺ complexes based on the chemical bond overlap polarizability, J. Lumin. 170 (2016) 420–430.
- [22] E. Raczuk, B. Dmochowska, J. Samaszko-Fiertek, J. Madaj, Different Schiff bases - structure, importance and classification, Molecules 27 (2022).
- [23] W. Zafar, S.H. Sumrra, Z.H. Chohan, A review: Pharmacological aspects of metal based 1,2,4-triazole derived Schiff bases, Eur. J. Med. Chem. 222 (2021) 113602.
- [24] I.P. Ejidike, P.A. Ajibade, Transition metal complexes of symmetrical and asymmetrical Schiff bases as antibacterial, antifungal, antioxidant, and anticancer agents: Progress and prospects, Rev. Inorg. Chem. 35 (2015) 191–224.
- [25] A. Mobinikhaledi, N. Foroughifar, M. Khanpour, S. Ebrahimi, Synthesis of some novel Schiff bases containing 1,2,4-triazole ring, Eur. J. Chem. 1 (2010) 33–36.
- [26] R.A. Murcia, S.M. Leal, M.V. Roa, E. Nagles, A. Muñoz-Castro, J.J. Hurtado, Development of antibacterial and antifungal triazole chromium(III) and cobalt(II) complexes: Synthesis and biological activity evaluations, Molecules 23 (2018).
- [27] M.T. Kaczmarek, M. Zabiszak, M. Nowak, R. Jastrzab, Lanthanides: Schiff base complexes, applications in cancer diagnosis, therapy, and antibacterial activity, Coord. Chem. Rev. 370 (2018) 42–54.
- [28] S. Kagatikar, D. Sunil, Schiff bases and their complexes in organic light emitting diode application, J. Electron. Mater. 50 (2021) 6708–6723.
- [29] A.K. Satapathy, S.K. Behera, R. Kumar, K.L. Sandhya, C.V. Yelamaggad, B. Sahoo, Excited state intramolecular proton transfer emission in bent core liquid crystals, J. Photochem. Photobiol. A: Chem. 358 (2018) 186–191.
- [30] A.K. Satapathy, S.K. Behera, A. Yadav, L.N. Mahour, C. Yelamaggad, K. Sandhya, B. Sahoo, Tuning the fluorescence behavior of liquid crystal molecules containing Schiff-base: Effect of solvent polarity, J. Lumin. 210 (2019) 371–375.
- [31] J. Wu, W. Liu, J. Ge, H. Zhang, P. Wang, New sensing mechanisms for design of fluorescent chemosensors emerging in recent years, Chem. Soc. Rev. 40 (2011) 2482–2405
- [32] Q. Ain, S.K. Pandey, O.P. Pandey, S.K. Sengupta, Synthesis, spectroscopic, thermal and antimicrobial studies of neodymium(III) and samarium(III) complexes derived from tetradentate ligands containing N and S donor atoms, Spectrochim. Acta A 140 (2015) 27–34.
- [33] A. Vishwakarma, S.K. Sengupta, O.P. Pandey, Characterizations and photophysical properties of synthesized Europium(III) and Terbium(III) complexes with mercapto-triazole Schiff base ligands, J. Lumin. 229 (2021) 117659.
- [34] E. Kraka, W. Zou, Y. Tao, Decoding chemical information from vibrational spectroscopy data: Local vibrational mode theory, WIREs: Comput. Mol. Sci. 10 (2020) 1480.
- [35] R.T. Moura Jr., A.N. Carneiro Neto, E.C. Aguiar, C.V. Santos-Jr., E.M. de Lima, W.M. Faustino, E.E.S. Teotonio, H.F. Brito, M.C.F.C. Felinto, R.A.S. Ferreira, L.D. Carlos, R.L. Longo, O.L. Malta, (INVITED) JOYSpectra: A web platform for luminescence of lanthanides, Opt. Mater.: X 11 (2021) 100080.
- [36] R.T. Moura Jr., A.N. Carneiro Neto, O.L. Malta, R.L. Longo, Overlap properties of chemical bonds in generic systems including unusual bonding situations, J. Mol. Model. 26 (2020) 1–18.
- [37] C.V. Santos-Jr, E.M. Lima, R.T. Moura Jr., Numerical integration of overlap electron densities: Parallelization strategies for a good load balancing using OpenMP, Comput. Theor. Chem. 1206 (2021) 113457.

[38] W. Zou, Y. Tao, M. Freindorf, M.Z. Makoś, N. Verma, D. Cremer, E. Kraka, Local vibrational mode analysis (Imodea, 2021, Computational and Theoretical Chemistry Group (CATCO), Southern Methodist University: Dallas, TX, USA.

- [39] W.T. Carnall, H. Crosswhite, H.M. Crosswhite, Energy level structure and transition probabilities in the spectra of the trivalent lanthanides in LaF₃, 1978, https://www.osti.gov/biblio/6417825.
- [40] L. Blois, A.N.C. Neto, R.L. Longo, I.F. Costa, T.B. Paolini, H.F. Brito, O.L. Malta, On the experimental determination of 4f-4f intensity parameters from the emission spectra of Europium (III) compounds, Opt. Spectrosc. 130 (2022) 10–17.
- [41] O. Malta, Theoretical crystal-field parameters for the YOCl:Eu³⁺ system. A simple overlap model, Chem. Phys. Lett. 88 (1982) 353–356.
- [42] O. Malta, A simple overlap model in lanthanide crystal-field theory, Chem. Phys. Lett. 87 (1982) 27–29.
- [43] B.R. Judd, Ionic transitions hypersensitive to environment, J. Chem. Phys. 70 (1979) 4830–4833.
- [44] C.K. Jørgensen, B.R. Judd, Hypersensitive pseudoquadrupole transitions in lanthanides, Mol. Phys. 8 (1964) 281–290.
- [45] G.F. de Sá, O.L. Malta, C. de Mello Donegá, A.M. Simas, R.L. Longo, P.A. Santa-Cruz, E.F. da Silva, Spectroscopic properties and design of highly luminescent lanthanide coordination complexes, Coord. Chem. Rev. 196 (2000) 165–195.
- [46] B.R. Judd, Optical absorption intensities of rare-earth ions, Phys. Rev. 127 (1962) 750–761.
- [47] S.F. Mason, R.D. Peacock, B. Stewart, Ligand-polarization contributions to the intensity of hypersensitive trivalent lanthanide transitions, Mol. Phys. 30 (1975) 1829–1841.
- [48] G.S. Ofelt, Intensities of crystal spectra of rare-earth ions, J. Chem. Phys. 37 (1962) 511–520.
- [49] S.F. Mason, R.D. Peacock, B. Stewart, Dynamic coupling contributions to the intensity of hypersensitive lanthanide transitions, Chem. Phys. Lett. 29 (1974) 149–153.
- [50] A.N. Carneiro Neto, R.T. Moura Jr., E.C. Aguiar, C.V. Santos, M.A.F.L.B. de Medeiros, Theoretical study of geometric and spectroscopic properties of Eu(III) complexes with Ruhemann's Purple ligands, J. Lumin. 201 (2018) 451–459.
- [51] H.B. Bebb, A. Gold, Multiphoton ionization of hydrogen and rare-gas atoms, Phys. Rev. 143 (1966) 1–24.
- [52] O.L. Malta, E.A. Gouveia, Comment on the average energy denominator method in perturbation theory, Phys. Lett. A 97 (1983) 333–334.
- [53] V. Trannoy, A.N. Carneiro Neto, C.D.S. Brites, L.D. Carlos, H. Serier-Brault, Engineering of mixed Eu³⁺/Tb³⁺ metal-organic frameworks luminescent thermometers with tunable sensitivity, Adv. Opt. Mater. 9 (2021) 2001938.
- [54] R.T. Moura Jr., O.L. Malta, R.L. Longo, The chemical bond overlap plasmon as a tool for quantifying covalency in solid state materials and its applications to spectroscopy, Int. J. Quantum Chem. 111 (2011) 1626–1638.
- [55] L.D. Carlos, O.L. Malta, R.Q. Albuquerque, A covalent fraction model for lanthanide compounds, Chem. Phys. Lett. 415 (2005) 238–242.
- [56] P.R. Santos, D.K. Pereira, I.F. Costa, I.F. Silva, H.F. Brito, W.M. Faustino, A.N. Carneiro Neto, R.T. Moura, M.H. Araujo, R. Diniz, O.L. Malta, E.E. Teotonio, Experimental and theoretical investigations of the [Ln(β-dik)(NO₃)₂(phen)₂]·H₂o luminescent complexes, J. Lumin. 226 (2020) 117455.
- [57] A.N. Carneiro Neto, R.T. Moura Jr., Overlap integrals and excitation energies calculations in trivalent lanthanides 4f orbitals in pairs Ln-L (L=Ln, N, O, F, P, S, Cl, Se, Br, and I), Chem. Phys. Lett. 757 (2020) 137884.
- [58] Z. Konkoli, D. Cremer, A New Way of Analyzing Vibrational Spectra. I. Derivation of Adiabatic Internal Modes, Int. J. Quantum Chem. 67 (1998) 1–9.
- [59] Z. Konkoli, J.A. Larsson, D. Cremer, A new way of analyzing vibrational spectra. II. Comparison of internal mode frequencies, Int. J. Quantum Chem. 67 (1998) 11–27.
- [60] Z. Konkoli, D. Cremer, A new way of analyzing vibrational spectra. III. Characterization of normal vibrational modes in terms of internal vibrational modes, Int. J. Quantum Chem. 67 (1998) 29–40.
- [61] Z. Konkoli, J.A. Larsson, D. Cremer, A new way of analyzing vibrational spectra. IV. Application and testing of adiabatic modes within the concept of the characterization of normal modes, Int. J. Quantum Chem. 67 (1998) 41–55.
- [62] D. Cremer, J.A. Larsson, E. Kraka, New developments in the analysis of vibrational spectra on the use of adiabatic internal vibrational modes, in: C. Parkanyi (Ed.), Theoretical and Computational Chemistry, Elsevier, Amsterdam, 1998, pp. 259–327.
- [63] E.B. Wilson, J.C. Decius, P.C. Cross, Molecular Vibrations: The Theory of Infrared and Raman Vibrational Spectra, McGraw-Hill, 1955.
- [64] L.A. Woodward, Introduction to the Theory of Molecular Vibrations and Vibrational Spectroscopy, Oxford University Press, Oxford, 1972.
- [65] G. Herzberg, Molecular Spectra and Molecular Structure, Vol. I, second ed., Reitell Press, New York, 2008.
- [66] G. Herzberg, Molecular Spectra and Molecular Structure. Volume II: Infrared and Raman Spectra of Polyatomic Molecules, Krieger Publishing Co, New York, 1991.
- [67] G. Herzberg, K.P. Huber, Molecular Spectra and Molecular Structure, in: IV. Constants of Diatomic Molecules, Van Nostrand, Reinhold, New York, 1979.
- [68] S. Califano, Vibrational States, Wiley, New York, 1976.

- [69] R.J. Meier, Calculating the vibrational spectra of molecules: An introduction for experimentalists with contemporary examples, Vib. Spectros. 43 (2007) 26–37.
- [70] W. Zou, D. Izotov, D. Cremer, New way of describing static and dynamic deformations of the Jahn-Teller type in ring molecules, J. Phys. Chem. A 115 (2011) 8731–8742.
- [71] W. Zou, M. Filatov, D. Cremer, Bond pseudorotation, Jahn-Teller, and Pseudo-Jahn-Teller effects in the cyclopentadienyl cation and its pentahalogeno derivatives, Int. J. Quantum Chem. 112 (2012) 3277–3288.
- [72] W. Zou, D. Cremer, Description of bond pseudorotation, bond pseudolibration, and ring pseudoinversion processes caused by the Pseudo-Jahn-Teller effect: Fluoro derivatives of the cyclopropane radical cation, Aust. J. Chem. 67 (2014) 435
- [73] D. Cremer, J.A. Pople, General definition of ring puckering coordinates, J. Am. Chem. Soc. 97 (1975) 1354–1358.
- [74] V. Barone, S. Alessandrini, M. Biczysko, J.R. Cheeseman, D.C. Clary, A.B. Mc-Coy, R.J. DiRisio, F. Neese, M. Melosso, C. Puzzarini, Computational molecular spectroscopy, Nat. Rev. Methods Primers 1 (2021) 1–27.
- [75] C.R. Baiz, B. Błasiak, J. Bredenbeck, M. Cho, J.-H. Choi, S.A. Corcelli, A.G. Dijkstra, C.-J. Feng, S. Garrett-Roe, N.-H. Ge, M.W.D. Hanson-Heine, J.D. Hirst, T.L.C. Jansen, K. Kwac, K.J. Kubarych, C.H. Londergan, H. Maekawa, M. Reppert, S. Saito, S. Roy, J.L. Skinner, G. Stock, J.E. Straub, M.C. Thielges, K. Tominaga, A. Tokmakoff, H. Torii, L. Wang, L.J. Webb, M.T. Zanni, Vibrational spectroscopic map, vibrational spectroscopy, and intermolecular interaction, Chem. Rev. 120 (2020) 7152–7218.
- [76] K.B. Beć, J. Grabska, C.W. Huck, Current and future research directions in computer-aided near-infrared spectroscopy: A perspective, Spectrochim. Acta A Mol. Biomol. Spectrosc. 254 (2021) 1–11.
- [77] E.B. Wilson, Some mathematical methods for the study of molecular vibrations, J. Chem. Phys. 9 (1941) 76–84.
- [78] W. Zou, R. Kalescky, E. Kraka, D. Cremer, Relating normal vibrational modes to local vibrational modes with the help of an adiabatic connection scheme, J. Chem. Phys. 137 (2012) 084114.
- [79] W. Zou, R. Kalescky, E. Kraka, D. Cremer, Relating normal vibrational modes to local vibrational modes: Benzene and naphthalene, J. Mol. Model. 19 (2012) 2865–2877.
- [80] J.C. Decius, Compliance matrix and molecular vibrations, J. Chem. Phys. 38 (1963) 241–248.
- [81] W. Zou, Y. Tao, M. Freindorf, D. Cremer, E. Kraka, Local vibrational force constants - From the assessment of empirical force constants to the description of bonding in large systems, Chem. Phys. Lett. 478 (2020) 137337.
- [82] R. Kalescky, E. Kraka, D. Cremer, Local vibrational modes of the formic acid dimer - The strength of the double H-bond, Mol. Phys. 111 (2013) 1497–1510.
- [83] R. Kalescky, E. Kraka, D. Cremer, New approach to Tolman's electronic parameter based on local vibrational modes. Inorg. Chem. 53 (2013) 478–495.
- [84] N. Verma, Y. Tao, W. Zou, X. Chen, X. Chen, M. Freindorf, E. Kraka, A critical evaluation of vibrational stark effect (VSE) probes with the local vibrational mode theory, Sensors 20 (2020) 2358.
- [85] G.B.V. Lima, J.C. Bueno, A.F. da Silva, A.N. Carneiro Neto, R.T. Moura, E.E.S. Teotonio, O.L. Malta, W.M. Faustino, Novel trivalent europium β-diketonate complexes with N-(pyridine-2-yl)amides and N-(pyrimidine-2-yl)amides as ancillary ligands: Photophysical properties and theoretical structural modeling, J. Lumin. 219 (2020) 116884.
- [86] P.N. Day, J.H. Jensen, M.S. Gordon, S.P. Webb, W.J. Stevens, M. Krauss, D. Garmer, H. Basch, D. Cohen, An effective fragment method for modeling solvent effects in quantum mechanical calculations, J. Chem. Phys. 105 (1996) 1968.
- [87] M.S. Gordon, M.W. Schmidt, Chapter 41 Advances in electronic structure theory: GAMESS a decade later, in: C.E. Dykstra, G. Frenking, K.S. Kim, G.E. Scuseria (Eds.), Theory and Applications of Computational Chemistry, Elsevier, 2005, pp. 1167–1189.
- [88] M.J. Frisch, G.W. Trucks, H.B. Schlegel, G.E. Scuseria, M.A. Robb, J.R. Cheeseman, G. Scalmani, V. Barone, G.A. Petersson, H. Nakatsuji, X. Li, M. Caricato, A.V. Marenich, J. Bloino, B.G. Janesko, R. Gomperts, B. Mennucci, H.P. Hratchian, J.V. Ortiz, A.F. Izmaylov, J.L. Sonnenberg, D. Williams-Young, F. Ding, F. Lipparini, F. Egidi, J. Goings, B. Peng, A. Petrone, T. Henderson, D. Ranasinghe, V.G. Zakrzewski, J. Gao, N. Rega, G. Zheng, W. Liang, M. Hada, M. Ehara, K. Toyota, R. Fukuda, J. Hasegawa, M. Ishida, T. Nakajima, Y. Honda, O. Kitao, H. Nakai, T. Vreven, K. Throssell, J.A. Montgomery, J.E. Peralta, F. Ogliaro, M.J. Bearpark, J.J. Heyd, E.N. Brothers, K.N. Kudin, V.N. Staroverov, T.A. Keith, R. Kobayashi, J. Normand, K. Raghavachari, A.P. Rendell, J.C. Burant, S.S. Iyengar, J. Tomasi, M. Cossi, J.M. Millam, M. Klene, C. Adamo, R. Cammi, J.W. Ochterski, R.L. Martin, K. Morokuma, O. Farkas, J.B. Foresman, D.J. Fox, Gaussian 16 Revision C.O1, 2016, Gaussian Inc. Wallingford CT.
- [89] T. Lu, F. Chen, Multiwfn: A multifunctional wavefunction analyzer, J. Comput. Chem. 33 (2012) 580–592.
- [90] O. Malta, Ligand-rare-earth ion energy transfer in coordination compounds. A theoretical approach, J. Lumin. 71 (1997) 229–236.
- [91] O.L. Malta, F.R. Gonçalves e Silva, A theoretical approach to intramolecular energy transfer and emission quantum yields in coordination compounds of rare earth ions, Spectrochim. Acta A 54 (1998) 1593–1599.

- [92] R. Longo, F.R. Gonçalves e Silva, O.L. Malta, A theoretical study of the energy-transfer process in [Eu⊂bpy.bpy.bpy]³⁺ cryptates: A ligand-to-metal charge-transfer state? Chem. Phys. Lett. 328 (2000) 67–74.
- [93] O. Malta, Mechanisms of non-radiative energy transfer involving lanthanide ions revisited, J. Non-Cryst. Solids 354 (2008) 4770–4776.
- [94] G.S. Ofelt, Structure of the F^6 Configuration with Application to Rare-Earth Ions, J. Chem. Phys. 38 (1963) 2171–2180.
- [95] E. Kasprzycka, A.N. Carneiro Neto, V.A. Trush, L. Jerzykiewicz, V.M. Amirkhanov, O.L. Malta, J. Legendziewicz, P. Gawryszewska, How minor structural changes generate major consequences in photophysical properties of RE coordination compounds; resonance effect, LMCT state, J. Rare Earths 38 (2020) 552–563.
- [96] J.F.C.B. Ramalho, L.M.S. Dias, L. Fu, A.M.P. Botas, L.D. Carlos, A.N. Carneiro Neto, P.S. André, R.A.S. Ferreira, Customized luminescent multiplexed quick-response codes as reliable temperature mobile optical sensors for ehealth and Internet of Things, Adv. Photonics Res. 3 (2022) 2100206.
- [97] S. Edvardsson, M. Klintenberg, Role of the electrostatic model in calculating rare-earth crystal-field parameters, J. Alloys Compd. 275–277 (1998) 230–233.
- [98] B. Judd, Operator Techniques in Atomic Spectroscopy, McGraw-Hill Book Company, 1998.
- [99] F.R.G. e Silva, O.L. Malta, Calculation of the ligand-lanthanide ion energy transfer rate in coordination compounds: Contributions of exchange interactions, J. Alloys Compd. 250 (1997) 427–430.
- [100] S. Sato, M. Wada, Relations between Intramolecular Energy Transfer Efficiencies and Triplet State Energies in Rare Earth β-diketone Chelates, Bull. Chem. Soc. Jpn. 43 (1970) 1955–1962.
- [101] E.E. Teotonio, H.F. Brito, G.F. de Sá, M.C.F. Felinto, R.H.A. Santos, R.M. Fuquen, I.F. Costa, A.R. Kennedy, D. Gilmore, W.M. Faustino, Structure and luminescent investigation of the Ln(III)-β-diketonate complexes containing tertiary amides, Polyhedron 38 (2012) 58–67.
- [102] E. Kasprzycka, A.N. Carneiro Neto, V.A. Trush, O.L. Malta, L. Jerzykiewicz, V.M. Amirkhanov, J. Legendziewicz, P. Gawryszewska, Spectroscopic aspects for the Yb³⁺ coordination compound with a large energy gap between the ligand and Yb³⁺ excited states, Spectrochim. Acta A 274 (2022) 121072.
- [103] A.N. Carneiro Neto, R.T. Moura, A. Shyichuk, V. Paterlini, F. Piccinelli, M. Bettinelli, O.L. Malta, Theoretical and experimental investigation of the Tb³⁺ → Eu³⁺ energy transfer mechanisms in cubic A₃Tb_{0.90}Eu_{0.10}(PO₄)₃ (A=Sr, Ba) materials. J. Phys. Chem. C 124 (2020) 10105–10116.
- [104] E. Hairer, G. Wanner, Radau methods, in: B. Engquist (Ed.), Encyclopedia of Applied and Computational Mathematics, Springer Berlin Heidelberg, Berlin, Heidelberg, 2015, pp. 1213–1216.
- [105] W.J.C. Grant, Role of rate equations in the theory of luminescent energy transfer, Phys. Rev. B 4 (1971) 648–663.
- [106] M. Fang, A.N.C. Neto, L. Fu, R.A.S. Ferreira, V. deZeaBermudez, L.D. Carlos, A hybrid materials approach for fabricating efficient WLEDs based on di-ureasils doped with carbon dots and a europium complex, Adv. Mater. Technol. 7 (2022) 2100727.
- [107] A.N. Carneiro Neto, E. Mamontova, A.M.P. Botas, C.D.S. Brites, R.A.S. Ferreira, J. Rouquette, Y. Guari, J. Larionova, J. Long, L.D. Carlos, Rationalizing the thermal response of dual-center molecular thermometers: The example of an Eu/Tb coordination complex. Adv. Opt. Mater. 10 (2022) 2101870.
- [108] D.M. Lyubov, A.N. Carneiro Neto, A. Fayoumi, K.A. Lyssenko, V.M. Korshunov, I.V. Taydakov, F. Salles, Y. Guari, J. Larionova, L.D. Carlos, J. Long, A.A. Trifonov, Employing three-blade propeller lanthanide complexes as molecular luminescent thermometers: Study of temperature sensing through a concerted experimental/theory approach, J. Mater. Chem. C 10 (2022) 7176–7188.
- [109] A.N. Carneiro Neto, E. Kasprzycka, A.S. Souza, P. Gawryszewska, M. Suta, L.D. Carlos, O.L. Malta, On the long decay time of the ⁷F₅ level of Tb³⁺, J. Lumin. 248 (2022) 118933.
- [110] J.-C.G. Bünzli, S.V. Eliseeva, Basics of lanthanide photophysics, in: P. Hänninen, H. Härmä (Eds.), Lanthanide Luminescence: Photophysical, Analytical and Biological Aspects, Springer Berlin Heidelberg, 2011, pp. 1–45.
- [111] K.-L. Wong, J.-C.G. Bünzli, P.A. Tanner, Quantum yield and brightness, J. Lumin. 224 (2020) 117256.
- [112] M. Safdar, A. Ghazy, M. Lastusaari, M. Karppinen, Lanthanide-based inorganicorganic hybrid materials for photon-upconversion, J. Mater. Chem. C 8 (2020) 6946–6965.
- [113] R. Sen, S. Paul, A. Sarkar, A.M.P. Botas, A.N. Carneiro Neto, P. Brandão, A.M.L. Lopes, R.A.S. Ferreira, J.P. Araújo, Z. Lin, A new series of 3D lanthanide phenoxycarboxylates: Synthesis, crystal structure, magnetism and photoluminescence studies, CrystEngComm 23 (2021) 4143–4151.
- [114] M.A.M. Filho, J.D.L. Dutra, G.B. Rocha, R.O. Freire, A.M. Simas, Sparkle/RM1 parameters for the semiempirical quantum chemical calculation of lanthanide complexes, RSC Adv. 3 (2013) 16747–16755.

- [115] J.J.P. Stewart, MOPAC2016, Stewart computational chemistry, 2016, http:// OpenMOPAC.net.
- [116] J. Gräfenstein, D. Cremer, Efficient density-functional theory integrations by locally augmented radial grids, J. Chem. Phys. 127 (2007) 164113.
- [117] J.-D. Chai, M. Head-Gordon, Long-range corrected hybrid density functionals with damped atom-atom dispersion corrections, Phys. Chem. Chem. Phys. 10 (2008) 6615–6620.
- [118] F. Weigend, R. Ahlrichs, Balanced basis sets of split valence, triple zeta valence and quadruple zeta valence quality for H to Rn: Design and assessment of accuracy, Phys. Chem. Chem. Phys. 7 (2005) 3297–3305.
- [119] M. Dolg, H. Stoll, H. Preuss, Energy-adjusted ab initio pseudopotentials for the rare earth elements, J. Chem. Phys. 90 (1989) 1730–1734.
- [120] E. Runge, E.K.U. Gross, Density-functional theory for time-dependent systems, Phys. Rev. Lett. 52 (1984) 997–1000.
- [121] J. Pipek, P.G. Mezey, A fast intrinsic localization procedure applicable for ab initio and semiempirical linear combination of atomic orbital wave functions, J. Chem. Phys. 90 (1989) 4916–4926.
- [122] A.D. Becke, A multicenter numerical integration scheme for polyatomic molecules, J. Chem. Phys. 88 (1988) 2547–2553.
- [123] E.E. Fileti, R. Rivelino, S. Canuto, Rayleigh light scattering of hydrogen bonded clusters investigated by means of ab initio calculations, J. Phys. B 36 (2003) 399–408.
- [124] W.M. Haynes, D.R. Lide, T.J. Bruno, CRC Handbook of Chemistry and Physics, ninetyseventh ed., CRC Press, 2016-2017.
- [125] A.S. McNeill, K.A. Peterson, D.A. Dixon, Polarizabilities of neutral atoms and atomic ions with a noble gas electron configuration, J. Chem. Phys. 153 (2020) 174304.
- [126] Y. Mei, A.C. Simmonett, F.C. Pickard, R.A. DiStasio, B.R. Brooks, Y. Shao, Numerical Study on the Partitioning of the Molecular Polarizability into Fluctuating Charge and Induced Atomic Dipole Contributions, J. Phys. Chem. A 119 (2015) 5865–5882.
- [127] E.F. Pettersen, T.D. Goddard, C.C. Huang, E.C. Meng, G.S. Couch, T.I. Croll, J.H. Morris, T.E. Ferrin, UCSF ChimeraX: Structure visualization for researchers, educators, and developers. Protein Sci. 30 (1) (2021) 70–82.
- [128] T.D. Goddard, C.C. Huang, E.C. Meng, E.F. Pettersen, G.S. Couch, J.H. Morris, T.E. Ferrin, UCSF ChimeraX: Meeting modern challenges in visualization and analysis, Protein Sci. 27 (2018) 14–25.
- [129] D. Cremer, E. Kraka, From molecular vibrations to bonding, chemical reactions, and reaction mechanism, Curr. Org. Chem. 14 (2010) 1524–1560.
- [130] E. Kraka, J.A. Larsson, D. Cremer, Generalization of the badger rule based on the use of adiabatic vibrational modes, in: J. Grunenberg (Ed.), Computational Spectroscopy, Wiley, New York, 2010, pp. 105–149.
- [131] E. Kraka, D. Setiawan, D. Cremer, Re-evaluation of the bond length-bond strength rule: The stronger bond is not always the shorter bond, J. Comput. Chem. 37 (2015) 130–142.
- [132] E. Kraka, D. Cremer, Weaker bonds with shorter bond lengths, Rev. Proc. Quim. (2012) 39–42.
- [133] E.V. Anslyn, D.A. Dougherty, Modern Physical Organic Chemistry, University Science Books, 2006.
- [134] R.D. Johnson III, NIST computational chemistry comparison and benchmark database - NIST standard reference database number 101, 2022, http://cccbdb. nist.gov/.
- [135] I. Bakó, D. Csókás, I. Mayer, S. Pothoczki, L. Pusztai, The influence of cations on the dipole moments of neighboring polar molecules, Int. J. Quantum Chem. 122 (2022) e26758.
- [136] M. Quintano, E. Kraka, Theoretical insights into the linear relationship between pK_a values and vibrational frequencies, Chem. Phys. Lett. 803 (2022) 139746.
- [137] A.N. Carneiro Neto, R.T. Moura Jr., L.D. Carlos, O.L. Malta, M. Sanadar, A. Melchior, E. Kraka, S. Ruggieri, M. Bettinelli, F. Piccinelli, Dynamic of the energy transfer process in Eu(III) complexes containing polydentate ligands based on pyridine, quinoline and iso-quinoline as chromophoric antennae, Inorg. Chem. 61 (2022) 16333–16346.
- [138] L. Blois, A.N. Carneiro Neto, O.L. Malta, H.F. Brito, The role of the $Eu^{3+} \, ^7F_1$ level in the direct sensitization of the 5D_0 emitting level through intramolecular energy transfer, J. Lumin. 247 (2022) 118862.